Clean Energy Science and Technology 2024, 2(3), 157.
https://doi.org/10.18686/cest.v2i3.157

Review

Recent progress of MoS_2 for photocatalytic and electrocatalytic hydrogen generation—A review

Liang Xu[1], Zhiguo Song[1], Hongkun Chen[2], Yongjin Li[1,*], Jingwei Li[3,*], Ruchun Li[2,*]

[1] Faculty of Materials Science and Engineering, Kunming University of Science and Technology, Kunming 650093, Yunnan Province, China
[2] Faculty of Chemistry and Chemical Engineering, Yunnan Normal University, Kunming 650500, Yunnan Province, China
[3] School of Chemistry and Chemical Engineering, Guangzhou University, Guangzhou 510006, Guangdong Province, China
*** Corresponding author:** Yongjin Li, liyongjin@kust.edu.cn; Jingwei Li, jingwei.li@gzhu.edu.cn; Ruchun Li, liruchun@ynnu.edu.cn

CITATION

Xu L, Song Z, Chen H, et al. Recent progress of MoS_2 for photocatalytic and electrocatalytic hydrogen generation—A review. Clean Energy Science and Technology. 2024; 2(3): 157. https://doi.org/10.18686/cest.v2i3.157

ARTICLE INFO

Received: 7 May 2024
Accepted: 12 August 2024
Available online: 19 September 2024

Abstract: Hydrogen (H_2) plays a crucial role in the transformation of the energy structure due to its environmental friendliness, renewability and high energy density. The photocatalytic and electrocatalytic hydrogen evolution reaction (HER) presents a promising approach for H_2 production. Molybdenum disulfide (MoS_2) has emerged as a promising catalyst in photocatalytic and electrocatalytic HER due to its high activity, easy preparation and cheapness. However, it suffers from poor stability and inactive basal planes. In this review, we encapsulated the research advancements of MoS_2 for photocatalytic and electrocatalytic HER in the past ~10 years. The latest strategies to enhance the catalytic activity of MoS_2, such as doping, phase adjustment, surface modification and others, are also summarized. The relationship between structure and activity for enhanced H_2 generation by different means is briefly introduced. The challenges and directions of MoS_2 materials in photocatalysis and electrocatalysis for HER are also discussed, aiming to provide promising guidelines for future research.

Keywords: photocatalysis; electrocatalysis; hydrogen evolution reaction; molybdenum disulfide

1. Introduction

Hydrogen (H_2) is considered as one of the options for the transformation of the future energy structure due to its advantages of being non-polluting and renewable and having a high energy density (142 $MJ \cdot kg^{-1}$), which holds the potential to replace fossil fuels and alleviate global warming and atmospheric pollution [1–5]. Moreover, H_2, as a highly combustible diatomic gas, is also the least dense gas [6]. Under standard conditions, the mass of H_2 is only 6.897% of the air mass at the same volume [7]. In addition, H_2 is the most common element in the universe with high volatility, high calorific value of combustion and high energy, which can be used as an energy carrier and fuel. At present, H_2 can be produced through fossil fuel conversion, biomass conversion and photocatalytic and electrocatalytic water electrolysis [4,8–10]. Among them, hydrogen evolution reaction (HER) via photocatalytic and electrocatalytic water electrolysis has been considered as the most potential method for efficient catalysis. Catalysts play a crucial role in photocatalytic and electrocatalytic HER processes [11–13]. Catalysts based on the noble metal Pt show an excellent HER property but their extensive application is severely limited by scarcity and high cost. Therefore, developing low-cost, highly active catalysts with attractive stability is of great significance.

Two-dimensional (2D) layered MoS_2 has received enormous attention due to its unique crystal structures and electronic and optical properties. MoS_2 has three tunable phases: 1T, 2H and 3R [14]. These properties allow MoS_2 as an excellent catalyst in various catalytic reactions, such as electrocatalysis and photocatalysis (**Scheme 1**). Previous works in the literature have confirmed that MoS_2 has active edge sites and inert basal planes [14,15]. However, the intrinsic activity of MoS_2 is restricted by its limited active edge sites. Therefore, new strategies to improve the intrinsic activity of 2D MoS_2 have aroused great research interest. Herein, the article focused on the recent research progress of MoS_2 for photocatalytic and electrocatalytic HER. The characteristics and modification methods of MoS_2 materials are introduced.

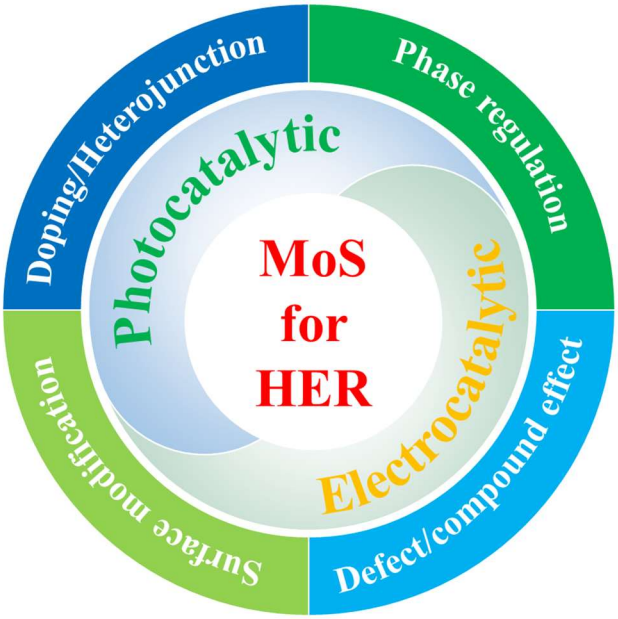

Scheme 1. Schematic highlight of MoS_2 for photocatalytic and electrocatalytic HER.

2. Structural feature

Generally, MoS_2 contains three different phase structures of 1T, 2H and 3R, where T, H and R represent tetragonal, hexagonal and rhombohedral, respectively, while the numbers 1, 2 and 3 indicate the number of layers in a unit cell, respectively, as shown in **Figure 1** [16]. Each MoS_2 monolayer is made up of three atomic layers with sandwiched molybdenum atoms between two layers of sulfur atoms. Generally, 1T-MoS_2 is metastable and possesses a single-layer atomic structure with octahedral metal coordination [17]. This structure leads to the metallic feature of 1T-MoS_2 in nature, meaning highly conductive. 2H-MoS_2 refers to a two-layer atomic structure with an adjacent monolayer spacing of 6–7 Å, where each layer is made up of a hexagonal arrangement of molybdenum atoms. 3R-MoS_2 is a rhombohedral structure with a band gap of 1.415 eV. However, 3R-MoS_2 is unstable at ambient temperature, which limits research on its reactivity. Interestingly, bulk MoS_2 is composed of multiple monolayers with weak van der Waals interactions, making them easy to separate. The adjacent monolayer distance can be tuned via chemical, electrochemical and solvothermal/hydrothermal methods. In addition, MoS_2 with different phases can

provide many unique features by constructing active unsaturated S/Mo atoms [14]. These enable MoS_2 to be utilized in various energy-related fields, including electrocatalysis, photocatalysis, rechargeable batteries, supercapacitors, fuel cells, etc. [18–21]. In this paper, the recent progress in photocatalytic and electrocatalytic HER is discussed.

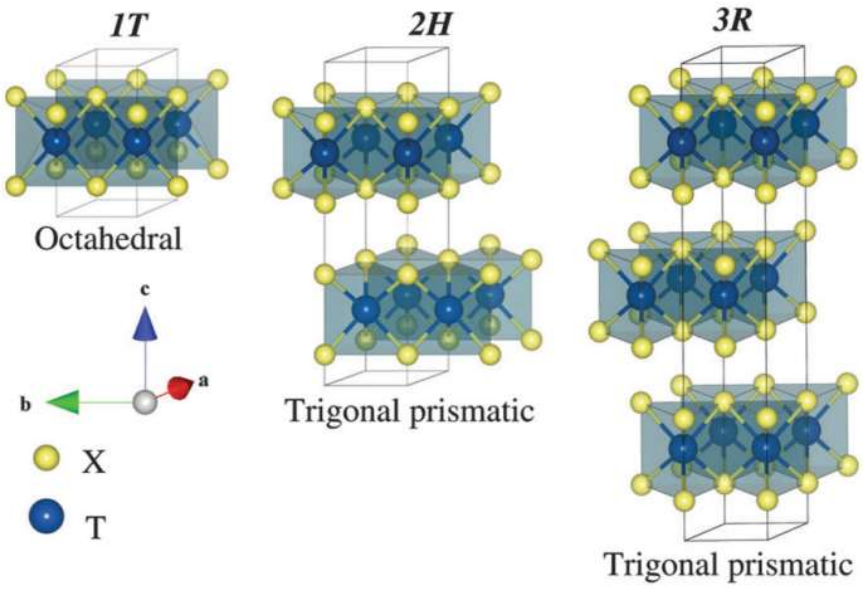

Figure 1. Structures of MoS_2: 1T, 2H and 3R [16].

3. Recent progress of photocatalytic HER

Photocatalysis is a chemical reaction in which a substance is converted by the combined action of light energy and a catalyst. Since the discovery of light-assisted decomposition of water via TiO_2 electrode by Fujishima and Honda in 1972 [22], many photocatalysts have been developed to promote photocatalytic HER. Currently, photocatalytic technology has been widely studied in the fields of hydrogen preparation, pollutant degradation, CO_2 reduction, antimicrobial and air purification [23–28]. Among them, photocatalytic hydrogen production is an environmentally friendly and promising technology to obtain hydrogen by decomposing water through light energy and catalysts, and it has received increasing attention. As shown in **Figure 2**, there are many similarities between photocatalysis and plant photosynthesis, as both undertake material transformation under sunlight and decompose water [29]. The energy required for photocatalytic HER comes from solar energy, which is clean, harmless and easy to obtain, and the required device has a simple structure and no secondary pollution and is easy to control and very friendly to the environment [14]. Photocatalytic HER, however, is a very complex process. It is affected by the catalyst itself, such as the catalyst's crystal defects, particle size, morphology, specific surface area, interface barrier, etc. In addition, it is influenced by external environmental factors during the photocatalytic process, such as the light source, reaction temperature, pH value, stirring speed and so on [30,31].

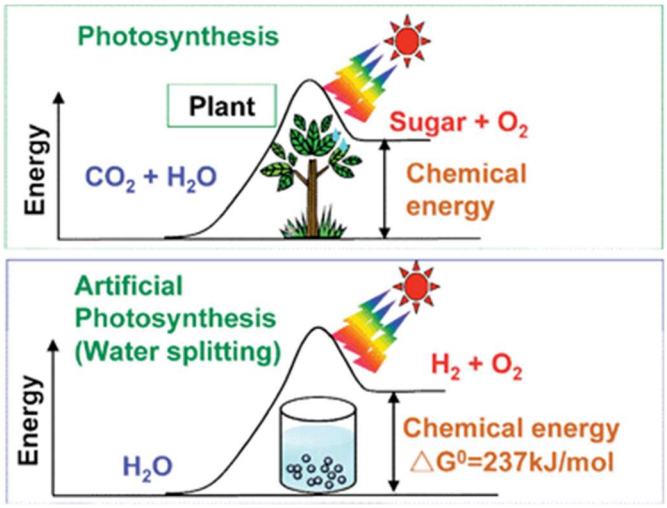

Figure 2. Diagram of natural photosynthesis and artificial photochemical reaction [29].

3.1. Fundamentals of photocatalytic HER

The hydrogen evolution reaction of semiconductor photocatalysts can be roughly simplified as the following processes [29]:

1) Absorption of incident light and photo-generated charge separation: When the photon energy of the incident light is greater than or equal to the band gap of a semiconductor catalyst, the semiconductor is photoexcited to produce electrons (photogenerated electron carriers) in the valence band, which transition to the conduction band of the semiconductor, thus leaving positively charged holes (photogenerated hole carriers) in the valence band.
2) Photogenerated electrons and holes migrate to active sites on the surface of the semiconductor: The process of electron and hole separation and migration is also related to the structure, crystallinity and grain size of the photocatalyst. The higher the crystallinity of the crystal, the fewer the defects. Defects can trap photogenerated electrons or holes to inhibit recombination for improved photocatalytic activity, and excess defects will become the recombination center instead, resulting in the reduction of photocatalytic activity. In addition, the reduction of grain size can shorten the distance of photogenerated carriers' migration to the surface of the photocatalyst, reducing the recombination rate of photogenerated carriers in the process of migration and improving photocatalytic efficiency.
3) Redox reaction on the photocatalyst's surface: Photogenerated holes with oxidizing ability oxidize H_2O adsorbed on the semiconductor's surface to O_2 and H^+. Photogenerated electrons with reducing ability react with H^+ to produce hydrogen. The chemical reaction is affected by surface active sites and the surface area. A large specific surface area can provide more active sites for photogenerated carriers to participate in the redox reaction.

Semiconductor materials for photocatalytic hydrogen production also need to meet the requirements that the oxidation potential of the top of the valence band is higher than that of O_2/H_2O (1.23 eV), that the reduction potential of the bottom of the conduction band is lower than that of H^+/H_2 (0 V vs. NHE), and that the band gap

width is greater than 1.23 eV. According to Equation (1), the wavelength of a light source directly used for photocatalytic hydrogen production should be less than about 1000 nm.

$$\text{Band gap (eV)} = \frac{1240}{\lambda}\text{(nm)} \quad (1)$$

3.2. Recent progress of MoS_2 for photocatalytic HER

MoS_2 nanomaterials possess outstanding optical and electronic properties and have attracted huge attention. In photocatalysis, MoS_2 has been considered as a promising co-catalyst for HER [32,33]. Generally, the band gaps of MoS_2 materials are different, such as 1.2 eV for bulk MoS_2 and 1.9 eV for single-layer MoS_2 due to quantum confinement. Thus, the size and number of layers of MoS_2 could affect its band gap and consequently adjust its photocatalytic activity. In addition, MoS_2 has some disadvantages, including low stability, low conductivity and the fast recombination rate of photogenerated carriers during photocatalytic HER. To overcome these problems, researchers have tried a variety of approaches [34–36]. For instance, when MoS_2 as a co-catalyst is supported on CdS, the formation of p/n junctions and a large number of active sites of monolayer MoS_2 nanosheets can enhance photocatalytic efficiency [34,35]. Liu et al. [37] reported that active edge sites of MoS_2 can be more exposed via the construction of a vertical orientation of MoS_2. **Figure 3(a,b)** show the structures of TiO_2 nanofibers and MoS_2 nanosheets. For the construction of a TiO_2@MoS_2 heterostructure, MoS_2 nanosheets grow on TiO_2 nanofibers (**Figure 3(c,d)**). **Figure 3(e)** exhibits the schematic diagram of the TiO_2@MoS_2 heterostructure model. The vertically grown MoS_2 on TiO_2 nanofibers can expose a large number of active edge sites [37]. In the following subsections, details of improved strategies for MoS_2 for photocatalytic HER are summarized.

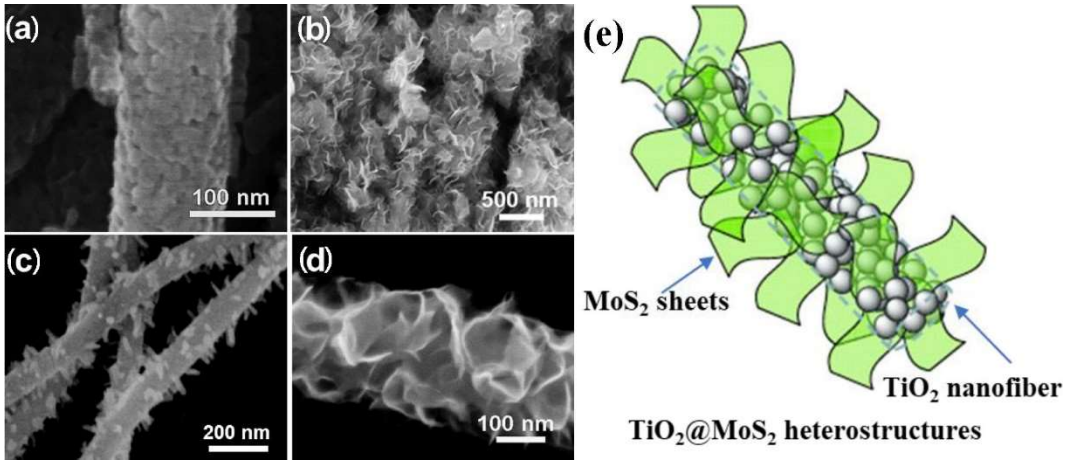

Figure 3. SEM images of **(a)** TiO_2 nanofibers, **(b)** pure MoS_2 nanosheets, **(c)** TiO_2@MoS_2 heterostructure after 12 h and **(d)** TiO_2@MoS_2 heterostructure after 24 h. **(e)** Schematic diagram of TiO_2@MoS_2 heterostructure model [37].

3.2.1. Doping

The progress of metal doping, non-metal doping and vacancy doping of MoS_2 was reviewed, and the effects of different types of doping on photocatalytic HER are summarized. It was found that doping can enlarge the light absorption range of a photocatalyst, increase its active sites, narrow its band gap, adjust its photogenerated

surface electron density, and reduce its charge transfer resistance [19,38–43]. Xue's team [38] prepared a co-catalyst of Co-doped MoS_x grown on TiO_2 nanoparticles using the photo-induction method and found that the formed highly active sites of "CoMoS" significantly improved HER activity. Co-MoS_2/g-C_3N_4 heterojunctions prepared by Wu et al. [19] improved the photocatalytic HER in a triethanolamine (TEOA) alkaline environment, where HER efficiency reached 3193 $\mu mol \cdot h^{-1} \cdot g^{-1}$. Co doping was found to change the local electronic structure and exposed more active sites. As shown in **Figure 4(a)**, the photoexcited electrons produced by g-C_3N_4 can move to the surface of Co-MoS_2, and the co-catalyst Co-MoS_2 can efficiently capture the photoinduced electrons and simultaneously provide active sites to activate hydrogen by reducing H_2O to H_2. The density functional theory (DFT) calculation revealed that Co doping not only distorts MoS_2 crystals but also reduces the H binding free energy of HER.

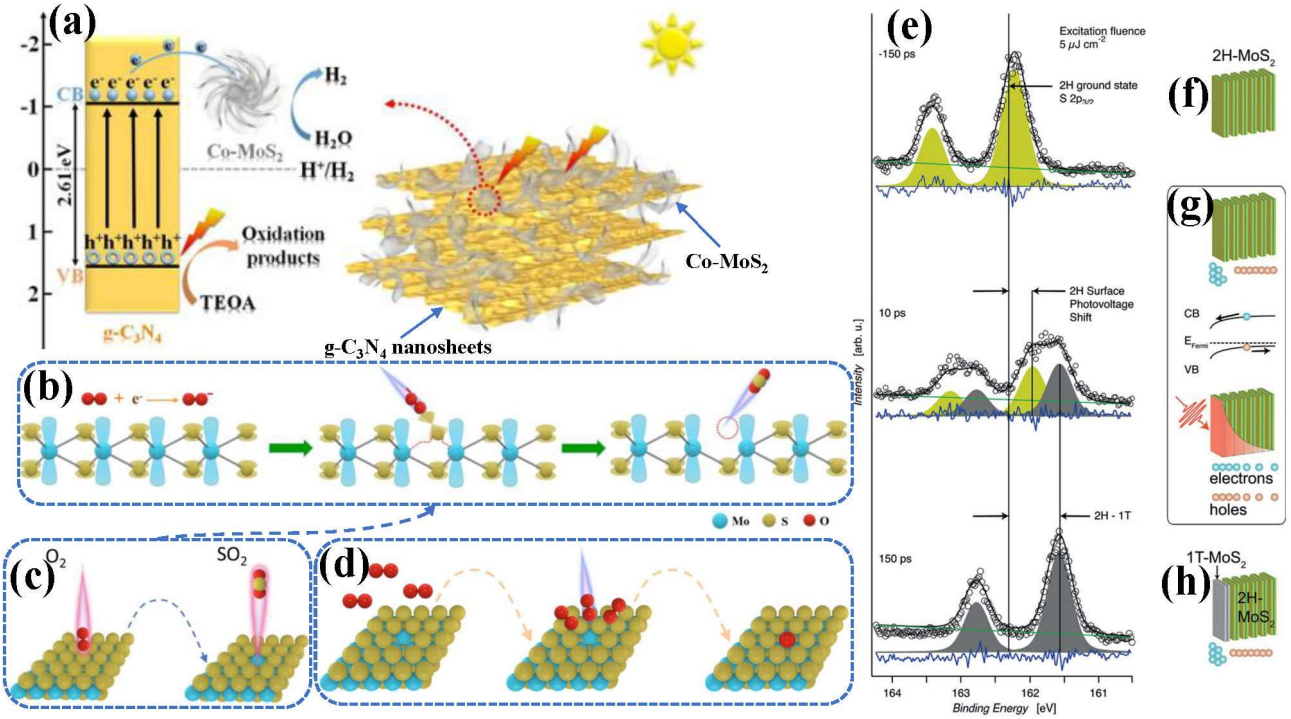

Figure 4. (a) Schematic illustration of photocatalytic mechanism of Co-MoS_2/g-C_3N_4 hybrids under simulated solar light irradiation [19]. **(b)** Schematic diagram of S vacancy formation triggered by external O_2 and electrons. **(c)** Schematic diagram of oxidation reaction during formation of S vacancy. **(d)** Schematic diagram of formation of $MoS_{2-x}O_x$ by oxygen occupying S vacancy in photocatalytic reaction [43]. **(e)** XPS spectra with laser excitation. **(f)** 2H-MoS_2 semiconductor. **(g)** Schematic diagram of creation of electron-hole pairs with exponential excitation profile from optical penetration depth. **(h)** Metallic 1T-MoS_2 phase on surface layer of 2H-MoS_2 [40].

In a study, the HER activity of Ni-doped flower-like MoS_2 was found to reach 404.3 $\mu mol \cdot h^{-1} \cdot g^{-1}$ [39]. Compared with undoped MoS_2, the doped sample had better charge separation and a stronger photoresponse at 600–700 nm. After six cycles of photocatalytic HER experiment, the hydrogen production of the photocatalyst maintained 95% of the initial hydrogen production. Sorgenfrei et al. [40] found that the energy band of the p-type doping of 2H-MoS_2 bent downward. The transient aggregation of surface electrons caused the transformation of the reversible 2H phase (semiconductor) into the 1T phase (metal) of the surface layer, which was completed

in only a few tens of picoseconds. As shown in **Figure 4(e)**, laser excitation from X-ray photoelectron spectroscopy (XPS) caused surface photovoltage shifts in p-doped 2H-MoS_2 (marked with yellow-green), as well as chemical shifts in the $S2p_{3/2}$ and $S2p_{1/2}$ core level lines of 1T-MoS_2 (marked with gray). After 150 ps of laser stimulation, the peak produced by the 2H phase completely disappeared, indicating that the surface layer was now completely in the metallic 1T phase. The semiconductor 2H-MoS_2 is shown in **Figure 4(f)**, while the metallic 1T-MoS_2 phase on 2H-MoS_2's surface layer is shown in **Figure 4(h)**. **Figure 4(g)** shows the electron-hole pairs and the exponential excitation curves generated by the light penetration depth, as well as the surface region separation of p-doped 2H-MoS_2, where electrons in the conduction band (denoted as CB) gather on the surface, while holes in the valence band (denoted as VB) migrate inward. The surface electron accumulation eventually produces and stabilizes the metallic 1T phase.

In addition, the entire basal plane of the 1T phase of MoS_2 has photocatalytic activity. Compared with the 2H phase, where only edge sites have photocatalytic activity, P-doped MoS_2 can improve HER efficiency under light irradiation. Using the hydrothermal method, Xin's team [41] prepared P-doped MoS_2, which showed stronger light absorption in the visible range, faster carrier transfer speed and lower resistance. The photocatalytic hydrogen production rate of P-doped MoS_2/CdS binary heterojunctions prepared by Xu et al. [42] in a mixed solution of Na_2S and Na_2SO_3 was 8.86 $mmol \cdot h^{-1} \cdot g^{-1}$. Studies have shown that P-doped heterojunctions have a more favorable band structure for photocatalytic HER.

Wang et al. [43] found that in the actual photocatalytic process, photogenerated electrons can induce slowly incoming pure oxygen to form active O_2^-. When O_2^- combines with S, the electron cloud is rearranged to break the Mo-S bond, forming SO_2 gas. Then, the SO_2 gas escapes from the surface of MoS_2, thus producing the S vacancy (**Figure 4(b,c)**). The continuous incoming pure oxygen in the environment fills the S vacancy (**Figure 4(d)**). In this way, MoS_2 is dynamically converted into $MoS_{2-x}O_x$, and oxygen elements can be well dispersed in MoS_2. The theoretical calculation showed that an appropriate amount of oxygen can make a sample undergo intrinsic deformation and optimize the surface's electronic state. In addition, the synergistic effect of strain engineering and O doping increases dynamic active sites on MoS_2 and decreases photogenerated charge transfer resistance.

3.2.2. Surface modification and morphology control

Generally, catalysis occurs at the surface of catalysts. Thus, the surface feature of catalysts plays an important role in efficient catalysis. The edge sites of MoS_2 have a low hydrogen adsorption free energy (ΔG_H^*) of 0.08 eV [44,45], which is comparable to those of many precious metal catalysts (**Figure 5(a,b)**), facilitating the desorption of hydrogen molecules on its surface. Li et al. [46] reported that strong local polarization occurred the surface of MoS_2 nanocrystals to promote charge separation by the introduction of polar-faceted metal oxides and layered double hydroxides (LDHs). The obtained catalyst (Ru:MoS_2/CeO_2 nanocrystals) showed a high HER activity of 2977 $\mu mol \cdot h^{-1} \cdot g^{-1}$ and quantum efficiency reaching 66.8% at 473 nm of visible light irradiation. The exciton lifetimes of the Ru-MoS_2 catalyst were much prolonged by the assembly with CeO_2 nanocrystals and MgO (111) and ZnO

nanoparticles (**Figure 5(c)**). When the Ru-MoS_2 catalyst was mixed with LDHs, the exciton lifetime increased (**Figure 5(d)**). The polarity of metal oxides was linearly related to exciton lifetime and photocatalytic activity. The exciton lifetime and photocatalytic HER ability increased as the polarity of the metal elements increased (**Figure 5(e,f)**).

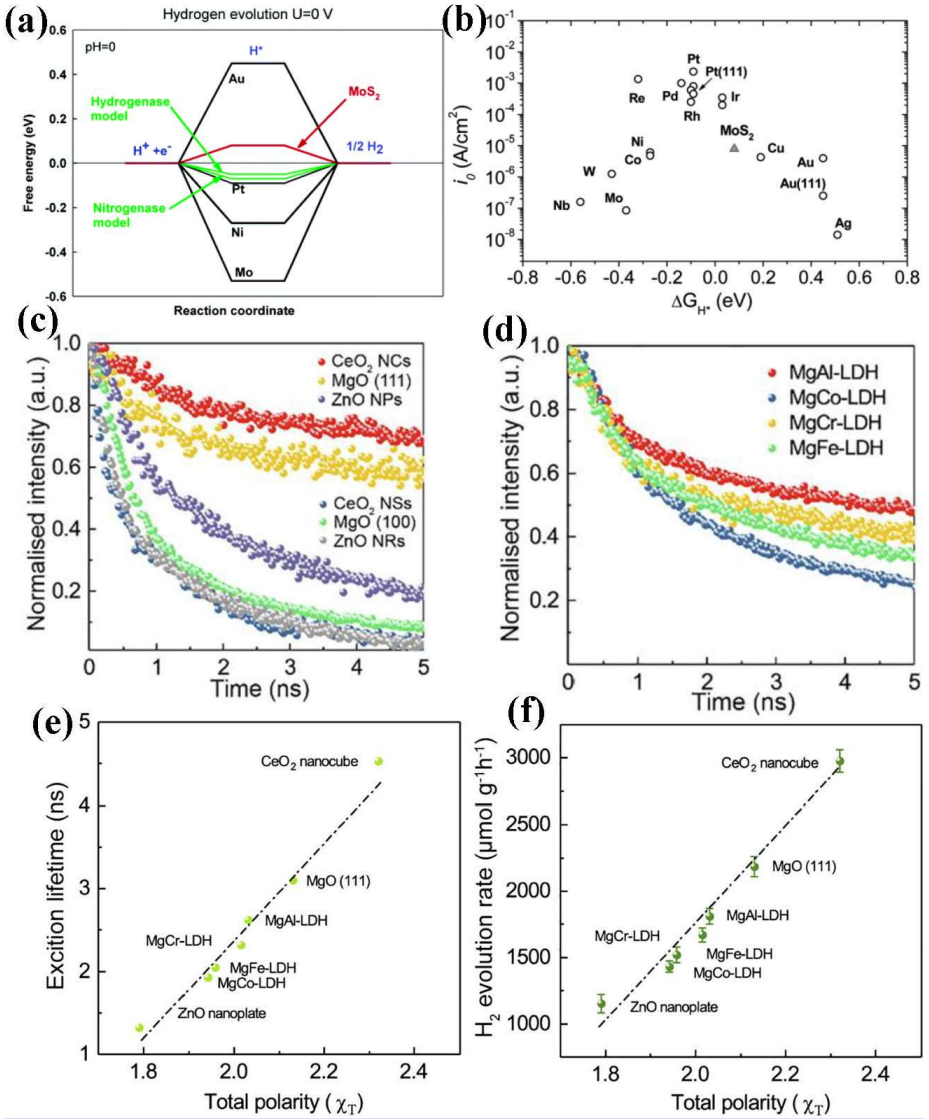

Figure 5. (a) Calculated free energy diagram for HER [45]. **(b)** Volcano plot of exchange current density as function of DFT-calculated Gibbs free energy of adsorbed atomic hydrogen for nanoparticulate MoS_2 and pure metals [44]. **(c)** Time-resolved photoluminescence spectra of Ru:MoS_2 mixed with polar-faceted oxide support. **(d)** Time-resolved photoluminescence spectra of Ru:MoS_2 mixed with non-polar-faceted oxide support. **(e)** Relationship between total polarity and exciton lifetimes. **(f)** Relationship between total polarity and photocatalytic HER activity [46].

In addition, a strategy to increase overall charge mobility has been proposed by using the exfoliation/etching method to expose more highly active edge sites [17]. Some studies have suggested that planar surface plasmon polaritons (SPPs) have a positive effect on the etching and thinning of MoS_2. MoS_2 can be etched into the required layer number and transverse dimension by controlling light power and incident direction [47]. This can be attributed to the reactive oxygen species produced

by plasma hot electrons weakening the interlayer interaction of MoS_2 and further promoting etching. **Figure 6(a)** shows the schematic illustration of inverted optical microscopy for triggering and monitoring the layer-controlled etching of MoS_2 nanoflakes. Excited SPPs are produced from the coupling of surface electromagnetic polaritons and oscillating free electrons propagated along the Au/water interface, generating an evanescent field with a penetration depth of approximately 200 nm. Atomic force microscopy (AFM) images of MoS_2 nanoflakes after etching (**Figure 6(b–d)**) indicate the decreased thicknesses of MoS_2. As shown in **Figure 6(e)**, time-varying optical images show that the direction of etching of MoS_2 nanosheets can be controlled by manipulating the direction of the propagation of the SPPs. Further studies have shown that the generated holes by exciton-plasma coupling in the valence band of MoS_2 lead to interlayer repulsion, while the generated electrons by plasma decay lead to interlayer dissolution. Liu et al. [48] proposed a local etching strategy, which realized the adjustment of the thickness and transverse size of MoS_2 (WS_2) and then adjusted the proportion of the photocatalyst's edges. Based on the method, the photocatalytic HER performance was 31 times and 47 times higher than those of unstripped MoS_2/CdS and WS_2/CdS, respectively. However, the preparation process of the local stripping method is relatively complicated and thus is not easy to be used for large-scale preparation.

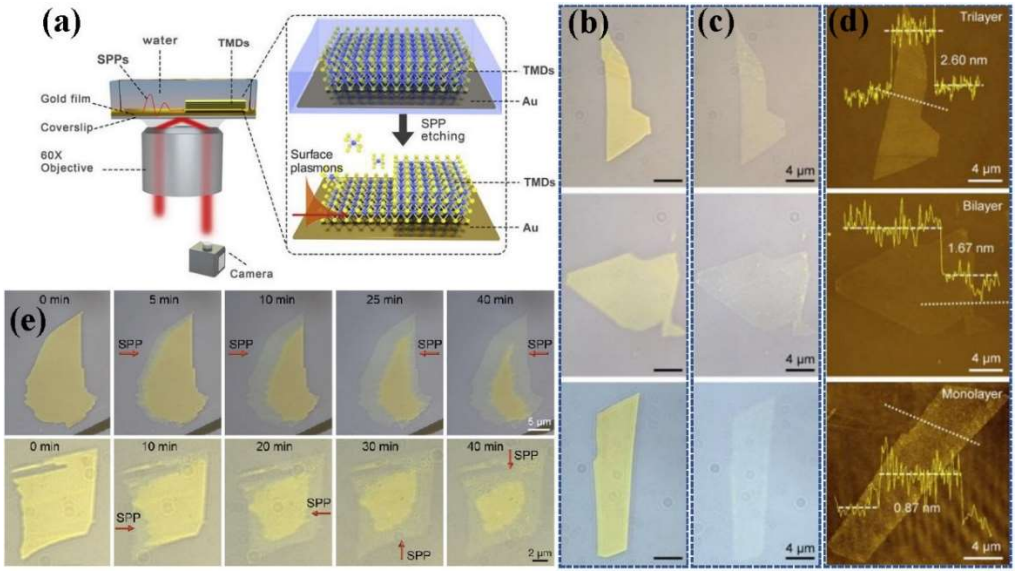

Figure 6. (a) Surface-plasmon-polariton-driven etching (SPPE) strategy. **(b)** Optical images of pristine exfoliated MoS_2 nanoflakes. **(c)** Optical images of MoS_2 nanoflakes after etching. **(d)** AFM images and corresponding height profiles of MoS_2 nanoflakes after etching. **(e)** Optical images of different etching directions [47].

It is well known that a photocatalyst with unique morphology can efficiently expose active sites and improve the charge transfer efficiency of the photocatalyst. Li's team [49] weakened the interlayer van der Waals forces of 1T-MoS_2 by controlling the number of -NH and -NH_2 intercalations and modulated the crystallinity and layer thickness of MoS_2. The HER efficiency of the obtained materials (P-1T-MoS_2/CdS) in lactic acid was 235.0 $mmol \cdot h^{-1} \cdot g^{-1}$ ($\lambda > 420$ nm), which was 2.25 times that of naked CdS under the same experimental condition. Nanometer flower-like MoS_2 loaded with Au particles was loaded on both ends of nanorod-like CdS to obtain

dumbbell symmetrical-tip heterojunctions, as shown in **Figure 7(a)**. This special structure allowed electrons to migrate directionally to the tip and accumulate, maintaining the long life of photogenerated carriers. The TEM images of typical Au/MoS_2-tipped CdS nanowires synthesized in an LA electrolyte (AMTC-LA) are shown in **Figure 7(b,d)**. The enlarged TEM image of the AMTC-LA in **Figure 7(c)** shows that Au nanoparticles with a diameter of ~10 nm were precisely deposited on the surface of MoS_2 tips, where the lattice spacing of Au was 0.23 nm (**Figure 7(d)**). Element mapping analyses demonstrated that the Au nanoparticles were concentrated on the tip of MoS_2, while Cd was present in only the stem (**Figure 7(e)**). High-resolution XPS data indicated two peaks at 84.8 and 88.5 eV appearing in the Au spectrum of the AMTC-LA, corresponding to metallic Au (**Figure 7(f)**). In addition, the energy barrier at the MoS_2/CdS interface was reduced by using an appropriate size of Au particles as a co-catalyst for photocatalytic HER electron transfer [50].

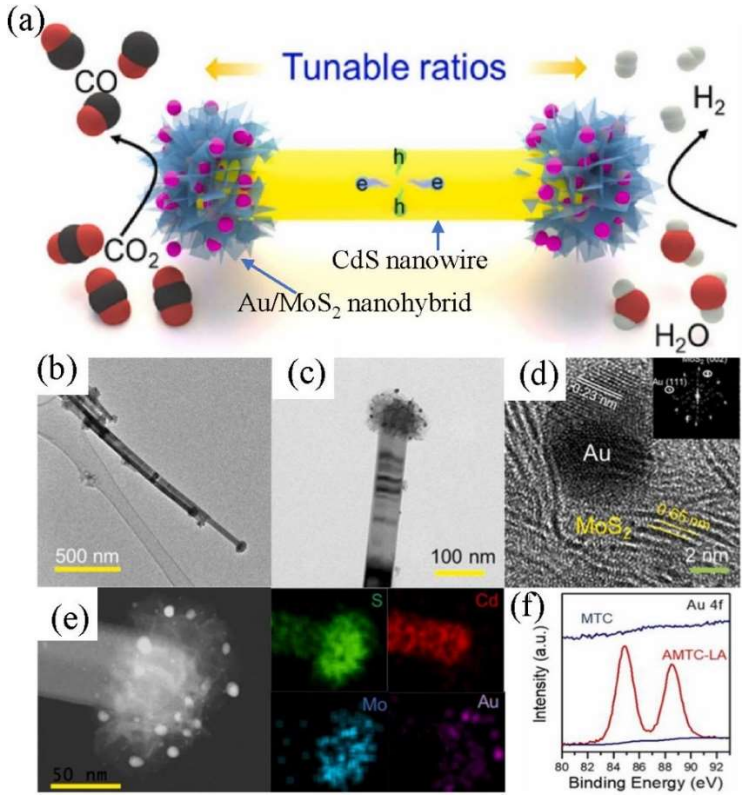

Figure 7. (a) Diagram of synthesis of dumbbell-shaped Au/MoS_2/CdS heterojunctions. **(b)** TEM image of Au/MoS_2-tipped CdS nanowires (AMTC-LA). **(c)** TEM image of AMTC-LA. **(d)** HR-TEM image of AMTC-LA (inset: fast Fourier transform pattern). **(e)** Element mapping of AMTC-LA. **(f)** XPS spectra of MTC and AMTC-LA [50].

3.2.3. Heterojunction construction

Previous studies have shown that the edge sites of monolayer MoS_2 are more stable than those of few-layer MoS_2, which is due to the increase of exciton binding energy and the decrease of carrier lifetimes caused by the transition from an indirect to a direct semiconductor [51]. From the construction of heterojunctions using MoS_2, the light absorption capacity in the visible range can be further increased and the band gap position of the composite can be adjusted to be more suitable for photocatalytic HER. For instance, Peng's team [52] showed HER enhancement of up to 40-fold

(compared with bare MoS_2) when the localized surface plasmon resonance (LSPR) wavelength of Au nanocages matched the absorption edge of MoS_2. With the aid of near-field enhancement, the energy of the surface plasma was transferred from Au nanocages to MoS_2 nanosheets, which promoted the electron-hole separation of MoS_2. By inserting a single layer of MoS_2 (ML-MoS_2) into a perovskite microcrystal nucleus by rapid recrystallization, Zhao's team [53] prepared ML-MoS_2/$MAPbI_3$ type II heterojunctions, in which each $MAPbI_3$ microcrystal (MC) anchored with multiple small-sized ML-MoS_2 nanosheets (**Figure 8(a)**). The obtained ML-MoS_2/$MAPbI_3$ MCs were uniformly sized rhombic dodecahedron-shaped MCs with an average size of 46 mm (**Figure 8(b,c)**). The surface photovoltage (SPV) diagram proved that the heterojunctions formed a strong internal electric field, which effectively inhibited charge recombination (**Figure 8(d)**). The ML-MoS_2/$MAPbI_3$ MCs showed a high hydrogen generation activity of 13.6 $mmol \cdot g_{Cat}^{-1} \cdot h^{-1}$ (**Figure 8(e)**). On the other hand, Guan's team [54] assembled MoS_2 nanoflowers and $MAPbI_3$ heterojunctions by colloidal precipitation. The results showed that the HER activity reached 29389 $\mu mol \cdot h^{-1} \cdot g^{-1}$ and the photocatalytic efficiency was 7.35%, outperforming those of $MAPbI_3$ perovskite.

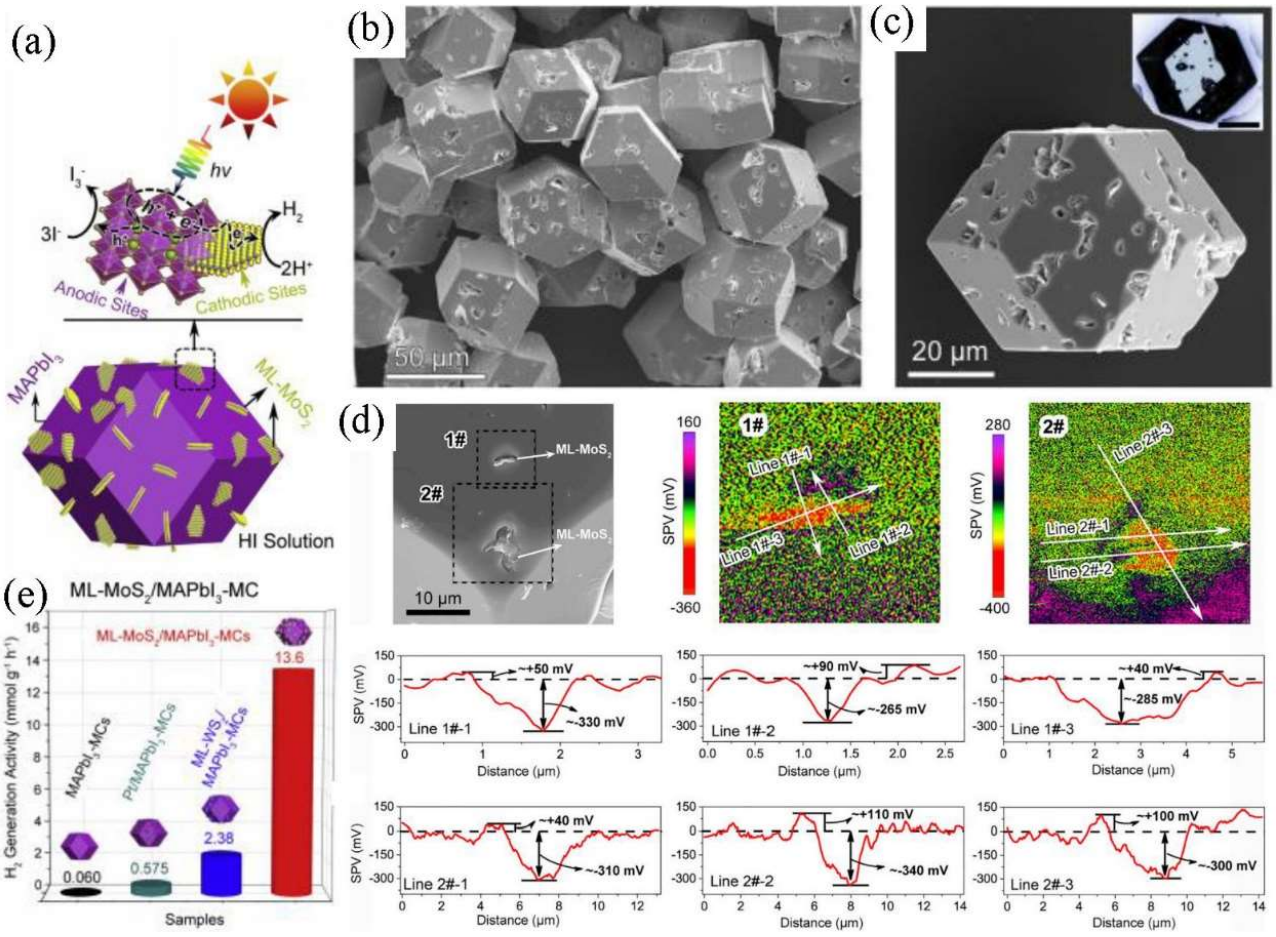

Figure 8. (a) Schematic illustration of structural configuration and redox processes of ML-MoS_2/$MAPbI_3$ MCs. **(b)** SEM image of ML-MoS_2/$MAPbI_3$ MCs. **(c)** SEM image of single ML-MoS_2/$MAPbI_3$ MC (inset: optical microscopy image with scale bar of 20 μm). **(d)** SPV distribution of ML-MoS_2/$MAPbI_3$ MCs. **(e)** Photocatalytic HER activity [53].

The photocatalytic HER efficiency of Bi_2O_3/MoS_2 heterojunction was shown to be 10 times higher than those of pure Bi_2O_3 and MoS_2 [55]. This was due to the expanded light absorption range. In addition, the Bi_2O_3/MoS_2 heterostructure formed p-n junctions, which had high-speed carrier transfer and can reduce the recombination of electrons and holes. Song et al. [56] prepared MoS_2/ReS_2@CdS heterojunctions with a hydrogen production rate of 171900 $\mu mol \cdot h^{-1} \cdot g^{-1}$. The photo-response range of ternary heterojunctions significantly improved, thanks to the dual-Z-scheme electron transfer mechanism of the ternary heterojunctions.

Furthermore, by intercalating Ti_3C_2 into MoS_2 layers, the two thin-sheet photocatalysts can be closely connected (**Figure 9(g)**) [57]. The scanning electron microscopy (SEM) images of the samples are presented in **Figure 9(a–e)**. The size of the initial MoS_2 spheres was approximately 1 μm (**Figure 9(a)**). Ti_3C_2 (**Figure 9(e)**) exhibited a clear multilayer structure, similar to that of exfoliated layered graphite. With the increase in Ti_3C_2 loading, MoS_2 completely covered the surface of the Ti_3C_2 layer (**Figure 9(b–d)**). As shown in **Figure 9(f)**, the photocatalytic HER activities of pure MoS_2 and Ti_3C_2 were poor. However, the combination of MoS_2 and Ti_3C_2 greatly enhanced catalytic activity (the loading amounts of Ti_3C_2 were 0 wt%, 10 wt%, 30 wt% and 50 wt% of the total mass, where the obtained samples were marked as T0, T10, T30 and T50, respectively). Especially, the T30 sample possessed a high photocatalytic HER rate of 6144.7 $mmol \cdot g^{-1} \cdot h^{-1}$, which was 2.3 times higher than that of pure MoS_2. This enhancement can be attributed to the presence of Ti_3C_2 promoting an efficient transfer of photogenerated electrons, indicating that the direction of charge transfer can be effectively controlled by a reasonable heterojunction design. In addition, CdS quantum dots were attached to MoS_2 nanosheets using a link assembly assisted by L-cysteine or mercaptoalkanoic acids. Ultrafast transient absorption measurements showed that the transfer of electrons from the quantum dots to the semiconductor was accomplished in 0.5–2 ps. The surfactant's functionalized quantum dot hole trap was located at the lower energy and closest to the edge of the valence band. By comparing the length of the surfactant's bridging distance, it was found that the reduction of the bridging distance accelerated the transfer speed of electrons between the quantum dots and the nanosheets [58]. Generally, $CuInS_2$ and Cu(In)S can effectively absorb light ranging from visible light to the near-infrared solar spectrum [59]. Vertical-epitaxial ultra-thin MoS_2 grown on the tip of a $CuInS_2$/CuS rod-like photocatalyst provided a large number of edge S sites (**Figure 10(a)**). TEM images of $CuInS_2$-CdS-MoS_2 HNs and $CuInS_2$-Cd(In)S-MoS_2 HNs (**Figure 10(b,c)**) revealed a rod-like structure. Furthermore, element mapping images (**Figure 10(d)**) displayed that S and In were distributed throughout the entire structure with Cd^--rich and Mo^--rich tips and Cu^--rich stems, indicating that In^{3+} partially migrated to the tip along with Cd^{2+} ion incorporation. Cross-arranged $CuInS_2$/Cu(In)S/MoS_2 Type II heterojunctions provided a good channel for electron transfer and also improved the stability of the photocatalytic materials. After 12 h of three cycles of photocatalysis, the HER activity, morphology, crystal structure, and chemical state of the sample remained good. In addition, $CuInS_2$/Cd(In)S/MoS_2 heterojunctions were prepared via cationic exchange from the tip Cu to Cd, and the photocatalytic HER reached 8000 $\mu mol \cdot h^{-1} \cdot g^{-1}$ (**Figure 10(e)**). Recently, researchers prepared quaternary heterojunctions by using mesoporous graphitic carbon nitride,

black phosphorus and molybdenum disulfide and incorporating Ni and Co co-catalysts (m-CN/BP/MoS_2-Y (Y: Ni, Co)), which formed Type I heterojunctions between BP and m-CN and formed Type II heterojunctions between m-CN and MoS_2, in addition to forming Type II heterojunctions between MoS_2 and BP [60]. The photogenerated electrons were transferred to Ni or Co to form H_2. The photocatalytic HER activity of the quaternary heterojunctions was 10 times higher than that of the BP/m-CN binary heterojunctions and 5 times higher than that of the m-CN/BP/MoS_2 ternary heterojunctions.

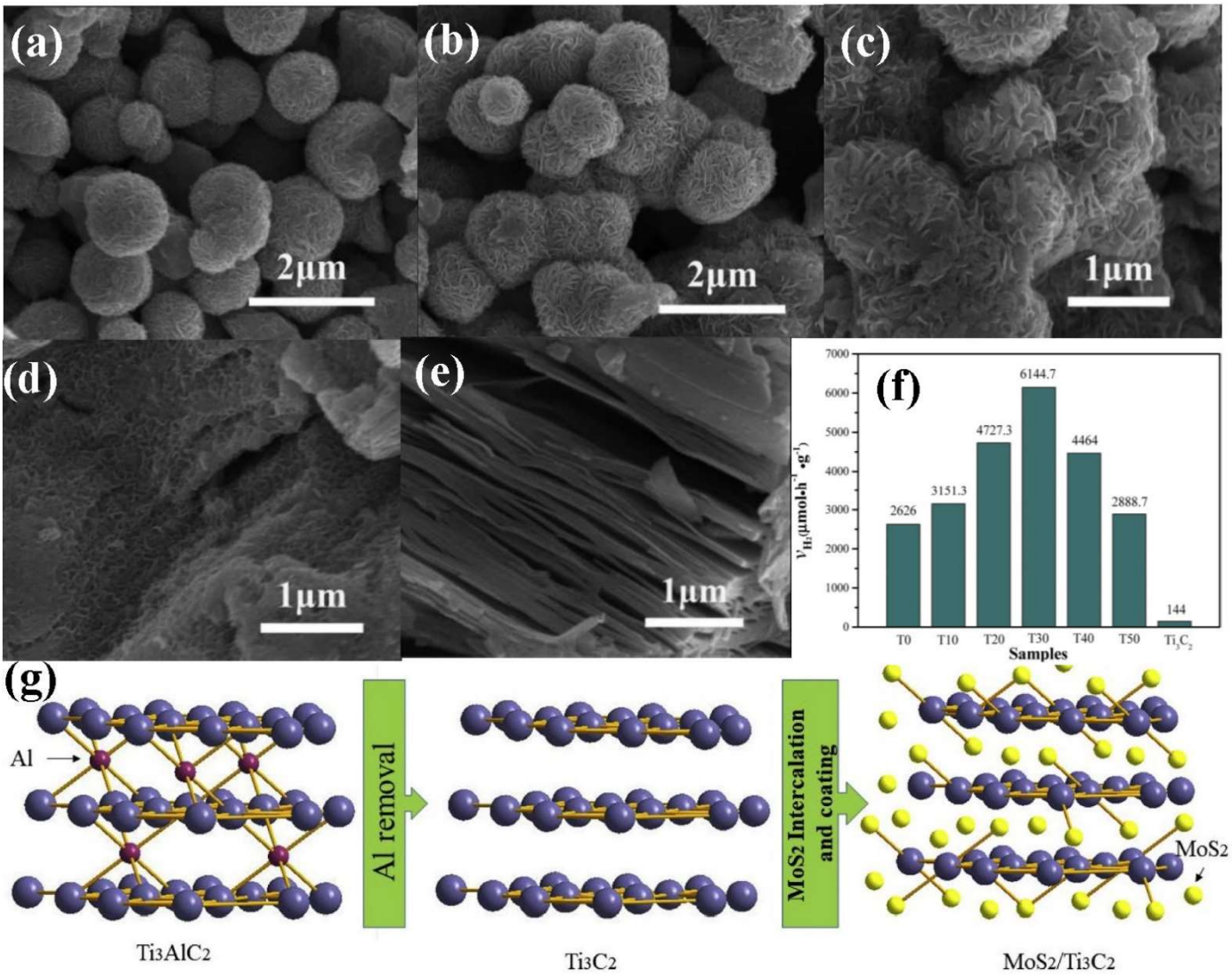

Figure 9. SEM images of MoS_2/Ti_3C_2 heterostructure synthesized at different Ti_3C_2 loading amounts: **(a)** T0, **(b)** T10, **(c)** T30, **(d)** T50 and **(e)** Ti_3C_2 MXene. **(f)** Photocatalytic H_2 production of Ti_3C_2 MXene and MoS_2/Ti_3C_2 heterostructures at different Ti_3C_2 loading amounts. **(g)** Schematic illustration of synthesis process of MoS_2/Ti_3C_2 heterostructure [57].

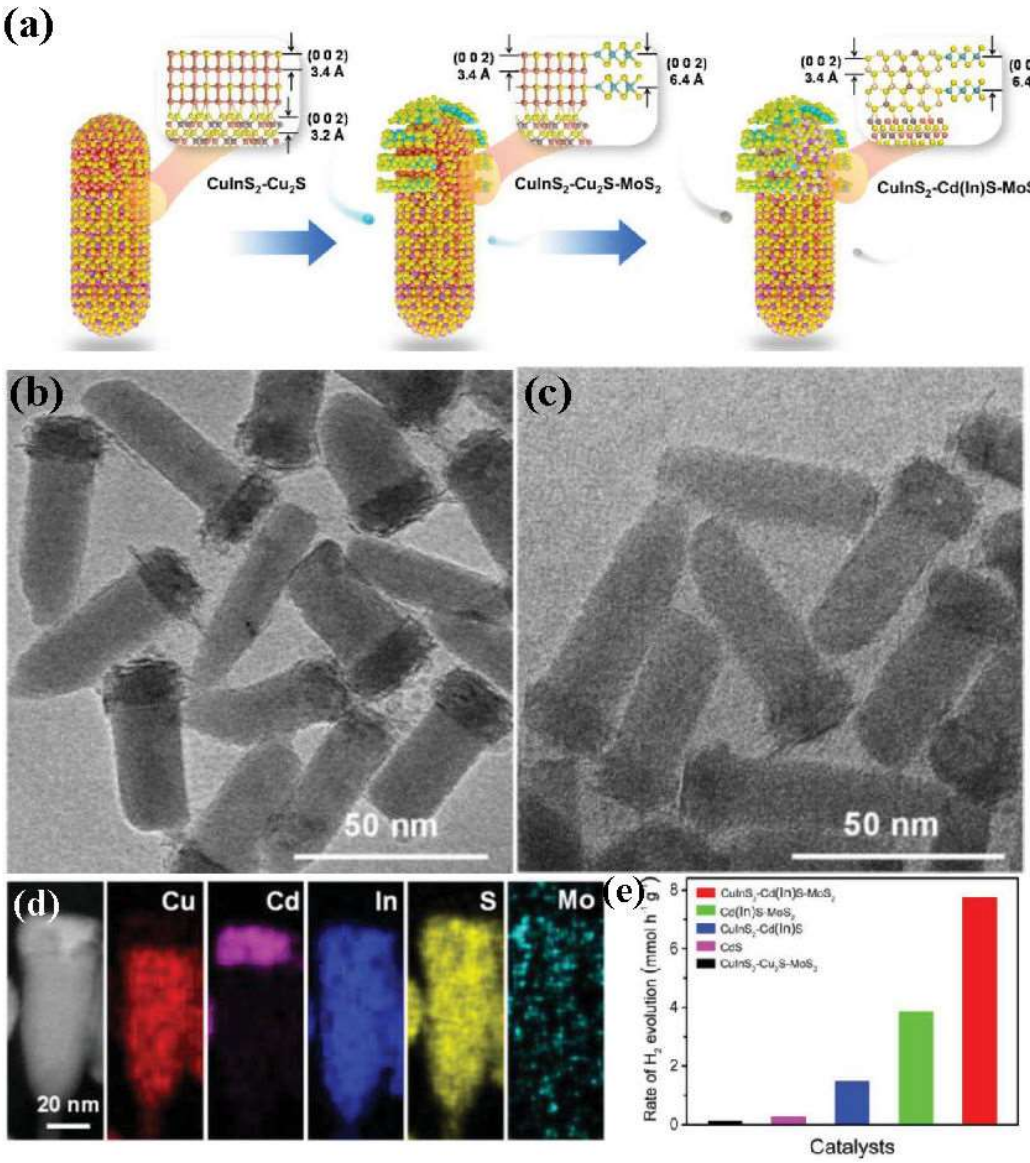

Figure 10. (a) Schematic illustration for selective epitaxial-hybrid of tripartite HNs. **(b)** TEM image of $CuInS_2$-Cu_2S-MoS_2 HNs. **(c)** TEM image of $CuInS_2$-Cd(In)S-MoS_2 HNs. **(d)** STEM-EDX elemental mapping images of single $CuInS_2$-Cd(In)S-MoS_2. **(e)** H_2 evolution rates of catalysts under visible light illumination ($\lambda > 420$ nm) [59].

3.2.4. Phase transformation

1T-MoS_2 and 2H-MoS_2 have been widely researched as catalysts. Compared with the conventional 2H-MoS_2 semiconductor, it is believed that 1T-MoS_2 with its metallic phase has abundant active sites at both its edges and basal planes, which can be used as adsorption and reaction sites of reactant molecules to accelerate reaction kinetics [61]. Previous reports have shown that P doping can convert the 2H semiconductor phase into the 1T metal phase of MoS_2 [40,41]. Das et al. [62] used a 532 nm laser to induce MoS_2 from a 2H phase to a 1T phase. Li's team [15] prepared 1T/2H-MoS_2 heterojunctions with a hydrogen production rate of 22.4 μmol·h^{-1} by adjusting the molar ratio of Mo/S via the hydrothermal method. The various methods for modifying MoS_2 to enhance its photocatalytic HER are summarized in **Table 1**.

Table 1. HER properties of modified MoS_2 photocatalysts.

Category	Photocatalyst	Synthesis method	Incident light (nm)	Light source	Activity ($\mu mol \cdot g^{-1} \cdot h^{-1}$)	Quantum yield (%)	Morphology	Ref.
Doping	Ni@MoS_2	Hydrothermal	λ = 420	Xe lamp (300 W)	404	-	Microflowers	[39]
	P-MoS_2	Hydrothermal	-	Xe lamp (300 W)	278.8	-	Interwoven nanosheets	[41]
	$MoS_{2-x}O_x$	Dynamic oxidation	λ > 420	Xe lamp (300 W)	1600	-	Nanosheets	[43]
Surface modification and morphology control	P-1T-MoS_2/CdS	Hydrothermal	λ > 420	Xe lamp (300 W)	235,000	49% at 420 nm	Nanosheets/ nanoflowers	[49]
	Au/MoS_2	Deposition	λ > 400	Hg lamp (200 W)	11,900	-	Nanoparticles	[52]
	MoS_2/ $MAPbI_3$	Colloidal precipitation	λ > 420	Xe lamp (280 W)	29,389	13.1% at 420 nm 22.1% at 500 nm	Rhombic dodecahedron-shaped microcrystals	[54]
Heterojunction construction	MoS_2/Ti_3C_2	Hydrothermal	λ > 420	Xe lamp (300 W)	6144.7	-	Flower-like nanosheets	[57]
	$CuInS_2$/Cd(In)S /MoS_2	Hot injection	λ > 420	Xe lamp (300 W)	8000	3.8% at 420 nm	Nanorods	[59]
	CuS–MoS_2-1T	Hydrothermal	λ > 300	Xe lamp (300 W)	9648.7	45.1% at 400 nm	Octahedrons	[63]
	O-1T/2H–MoS_2/g-C_3N_4	Hydrothermal	λ > 300	Xe lamp (500 W)	1487	7% at 370 nm	Nanosheets	[64]

Currently, various 1T-MoS_2-based heterojunctions have been developed for enhancing the catalytic performance of MoS_2. Octahedral CuS/1T-MoS_2 heterojunctions were formed by the in-situ growth of mesopore-structured 1T-MoS_2 in octahedral Cu metal-organic frameworks. **Figure 11(a)** shows the schematic illustration of the synthesis process of CuS-MoS_2-1T nanohybrid (via the confined template method) and CuS-MoS_2-2H nanohybrid (without confinement). The photocurrent density-time (I-t) curves in **Figure 11(b)** exhibited that CuS-MoS_2-1T generated the highest photocurrent because of the improved carrier transfer performance of 1T-MoS_2. As shown in **Figure 8(c)**, CuS-MoS_2-1T exhibited the smallest arc radius relative to those of CuS, 2H-MoS_2 and CuS–MoS_2–2H, attributed to the high electronic conductivity of 1T-MoS_2 [63]. The coupling of O-doped 1T/2H-MoS_2 and g-C_3N_4 increased the photocatalytic HER to 1487 $\mu mol \cdot h^{-1} \cdot g^{-1}$ because the metallic properties of the electronic structure of 1T-MoS_2 improved the electrical conductivity of the heterojunctions. The 1T-MoS_2 acted as an electron-trapping agent and promoted the separation of photogenerated charge carriers. In addition, the 1T-MoS_2 had a large number of HER active sites at both base and edge sites. In addition, the O doping of MoS_2 caused crystal distortion, thereby regulating the electronic structure [64].

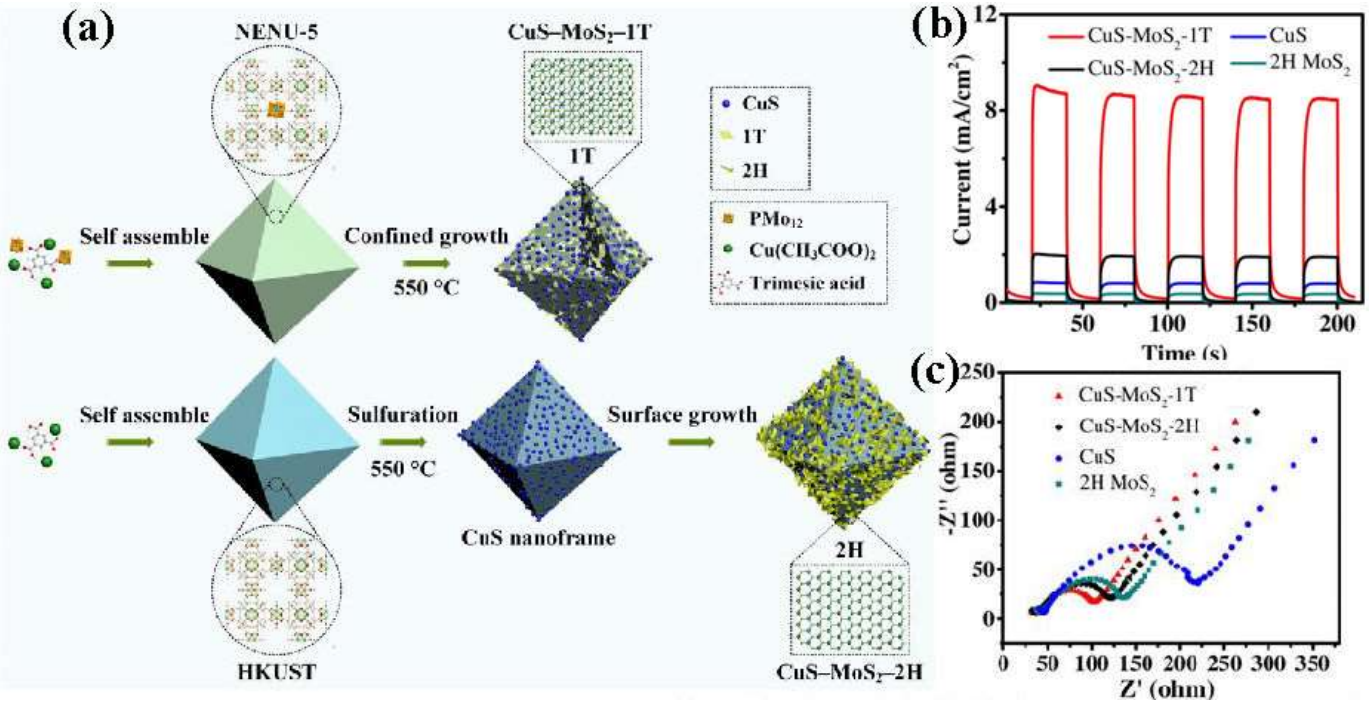

Figure 11. (a) Schematic illustration of synthesis process of CuS-MoS_2-1T and CuS-MoS_2-2H nanohybrids. **(b)** EIS Nyquist plots. **(c)** Photocurrent responses [63].

MoS_2 materials have great potential and research value in the field of photocatalytic HER, far beyond the capabilities demonstrated today. Although, at present, MoS_2 materials during photocatalytic HER suffer from some problems and challenges, such as competing spectral absorption range and redox potential, low photocatalytic efficiency, insufficient stability and fast photogenerated electron-hole recombination. However, with improvements in exploration methods and strategies and a better understanding of photocatalytic HER, MoS_2 materials have a broad future in the field of photocatalytic HER. In the future, high-throughput DFT predictions and the addition of large models of artificial intelligence will give more modifications and new properties of MoS_2 materials [65]. This will save researchers a lot of time and effort for experimental studies.

Improvements in preparation methods and a deep understanding of the photocatalytic HER mechanism of MoS_2 are very important. The purity of MoS_2 prepared via the wet chemical method is not as high as those prepared via other methods. MoS_2 synthesis of heterojunction materials can improve the light absorption range and accelerate electron-hole transfer [39]. Compared with flat MoS_2, wrinkled MoS_2 has faster electron relaxation [66]. It is generally believed that near-infrared light cannot directly excite MoS_2 catalysts to produce electrons and holes with sufficient energy to drive photocatalytic HER, but the infrared thermal effect can increase reaction temperature, mass transfer and the formation and breaking of chemical bonds in a catalytic reaction, thus contributing to a higher HER reaction rate [67]. In addition, the relationship between MoS_2's basal planes and edge sites, the change in its phase during photocatalysis and the transfer path of electrons are still unclear. Moreover, the formation mechanism and interface force of heterojunctions constructed by MoS_2 have not been reported. The large-scale and commercial application of photocatalytic MoS_2

materials is also one of the future development directions. For example, the total solar-hydrogen conversion efficiency of photocatalyzed HER via a hydrogen farm strategy was found to exceed 1.85% [68].

4. Recent progress of electrocatalytic HER

4.1. Mechanism of electrocatalytic HER

Electrochemical HER involves a two-electron transfer pathway, which can be expressed by following two steps: (1) the formation of adsorbed H intermediates (H*), called the Volmer step, and (2) H_2 generation from the combination of H*, called the Heyrovsky or Tafel step. In general, there are significant differences in the Volmer reaction in different pH environments (**Table 2**). In alkaline and neutral electrolytes, the Volmer reaction process needs to undergo water dissociation with H-OH breakthrough to form H* intermediates. The slow kinetics of water dissociation is a bottleneck for water electrolysis in an alkaline or neutral medium. In acidic electrolytes, the Volmer reaction can directly capture H^+ from electrolytes to form H* intermediates. Subsequently, H_2 may be produced through the Heyrovsky reaction or Tafel reaction, which is determined by the low or high coverage of H* intermediates, respectively. The true catalytic mechanism is mainly related to the surface element composition, surface roughness and electronic structure of the electrocatalyst. For the HER process, the Tafel slope is an efficient method to estimate the catalytic mechanism by the following equation (Equation (2)):

$$\eta = a + \mathrm{b} \log | j | \quad (2)$$

where η is the overpotential, j is the current density and b is the Tafel slope. The theoretical Tafel slope values for Volmer, Heyrovsky and Tafel reactions are 117, 39 and 29 $mV \cdot dec^{-1}$, respectively. It is worth noting, however, that the Tafel slopes of samples are different at various potential ranges, which implies that the HER mechanism changes at different potentials. Thus, the region for Tafel slope analysis is crucial for determining the HER mechanism and comparison with other reported materials.

Table 2. HER reaction mechanisms in alkaline, neutral and acidic media.

Alkiline and neutral meidia	Process	Acid media
$H_2O + * + e^- \rightarrow H^* + OH^-$	Volmer	$H^+ + * + e^- \rightarrow H^* + H_2O$
$H^* + H_2O + e^- \rightarrow * + OH^- + H_2$	Heyrovsky	$H^+ + H^* + e^- \rightarrow H_2 + * + H_2O$
$H^* + H^* \rightarrow * + H_2$	Tafel	$H^* + H^* \rightarrow * + H_2$

* represents active sites

4.2. Recent progress of MoS_2 for electrocatalytic HER

As a typical sulfide, MoS_2 has been widely used in many energy-related fields, such as electrocatalysis, battery, photocatalysis and thermocatalysis, due to its unique physical and chemical properties [69,70]. Especially, MoS_2 has emerged as a promising alternative to Pt-based electrocatalysts for HER due to its excellent catalytic activity and earth-abundance (**Scheme 2**). This is attributed to the favorable electronic structure of MoS_2, which allows for efficient adsorption and activation of H*

intermediates. Furthermore, MoS_2 can be easily synthesized via various methods using tunable morphologies, such as nanoparticles, nanosheets and nanospheres. Hinnemann et al. [45] were the first to find that Mo edges (1010) of MoS_2 have similar properties with hydrogenases and can produce stable H* intermediates. The theoretical calculations revealed that the unsaturated Mo edges of MoS_2 are crucial active sites for catalytic HER and has attractive free energy of H adsorption. The basal planes of MoS_2 are catalytically sluggish. The results confirmed MoS_2 as an HER electrocatalyst, and thus MoS_2 received great attention. Thereafter, Jaramillo and co-authors [44] identified the relationship between MoS_2's active sites for HER and electrocatalytic activity. They determined the surface sites of MoS_2 using scanning tunneling microscopy and then systematically tuned the active site distribution. The electrocatalytic results showed that the HER activity linearly correlated with the number of edge sites on MoS_2. Zhang et al. [71] also studied the origin of active sites in monolayer MoS_2. They found that its HER property positively related to Mo-terminated edge sites and the phase structure transition. The basal plane activity of 1T-MoS_2 was found to be beneficial to catalytic HER compared with that of 2H-MoS_2. Chen et al. [72] provided Raman spectroscopic evidence that confirmed the S−H bond formation on MoS_2's surface via in-situ Raman measurements. This suggests that S sites on the surface of MoS_2 can act as catalytically active sites for HER.

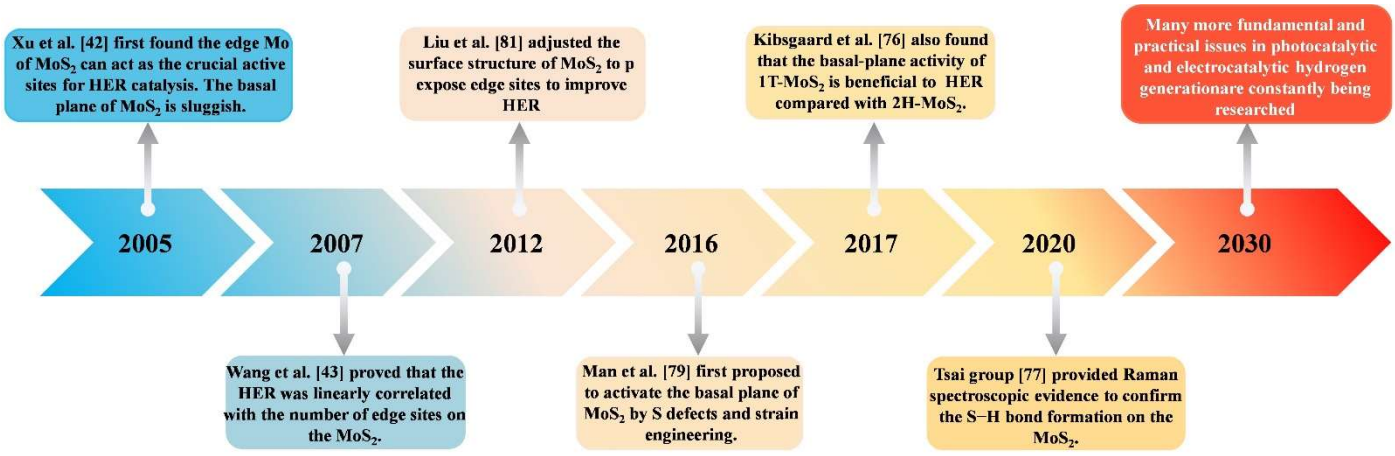

Scheme 2. Recent progress of MoS_2 for electrocatalytic HER.

Although MoS_2 has been confirmed as a potential candidate for an excellent electrocatalytic HER, its intrinsic activity still needs to be further enhanced compared with those of Pt-based electrocatalysts. Various methods, such as the exposure of edge sites, phase regulation, heterostructure construction, defect engineering, doping and compound effect, have been proposed to improve the catalytic HER activity of MoS_2.

4.2.1. Exposure of edge sites

Generally, MoS_2 contains active edge sites and inert basal planes. To enhance its catalytic HER activity, efficient strategies have been proposed to construct active edge sites on its inert basal planes [73–76]. Li et al. [74] were the first to propose activating the basal planes of 2H-MoS_2 by introducing S defects and strain engineering. The theoretical and experimental results revealed that the strained S vacancies were new active sites in the basal planes and that the free energy for H adsorption (ΔG_H) was

also tuned, contributing to the high intrinsic HER property. Hence, various S vacancies have been constructed using efficient methods to activate the basal planes of 2H-MoS_2. Tsai et al. [77] adopted electrochemical desulfurization to generate scalable S vacancies on the basal planes of MoS_2, which can be regulated by changing the applied desulfurization potential. The resulting stable active sites showed a good HER performance with a high per-site turnover frequency value. Liu and co-authors [78] employed point defects and vacancies to synergistically activate the inert basal planes of MoS_2 for improved HER performance. By combining on-chip electrochemical tests with theoretical calculations, they found that the type and amount of defect configurations played a crucial role in the catalytic HER. Man et al. [79] reported sulfur-vacancy-rich 2H-MoS_2 via a unique salt-assisted chemical vapor deposition method (**Figure 12(a)**). **Figure 12(b–d)** shows the distribution of sulfur vacancies and the corresponding strain maps. The vacancy density was controllably tuned with S vacancy ratios from 7.56% to 22.16%. In the strain maps, the strain value can be up to 14% with the increase in KCl concentration. The obtained MoS_2 exhibited a small overpotential of ≈158.8 mV at 100 mA·cm^{-2} in an acid electrolyte, outperforming previously reported MoS_2-based electrocatalysts.

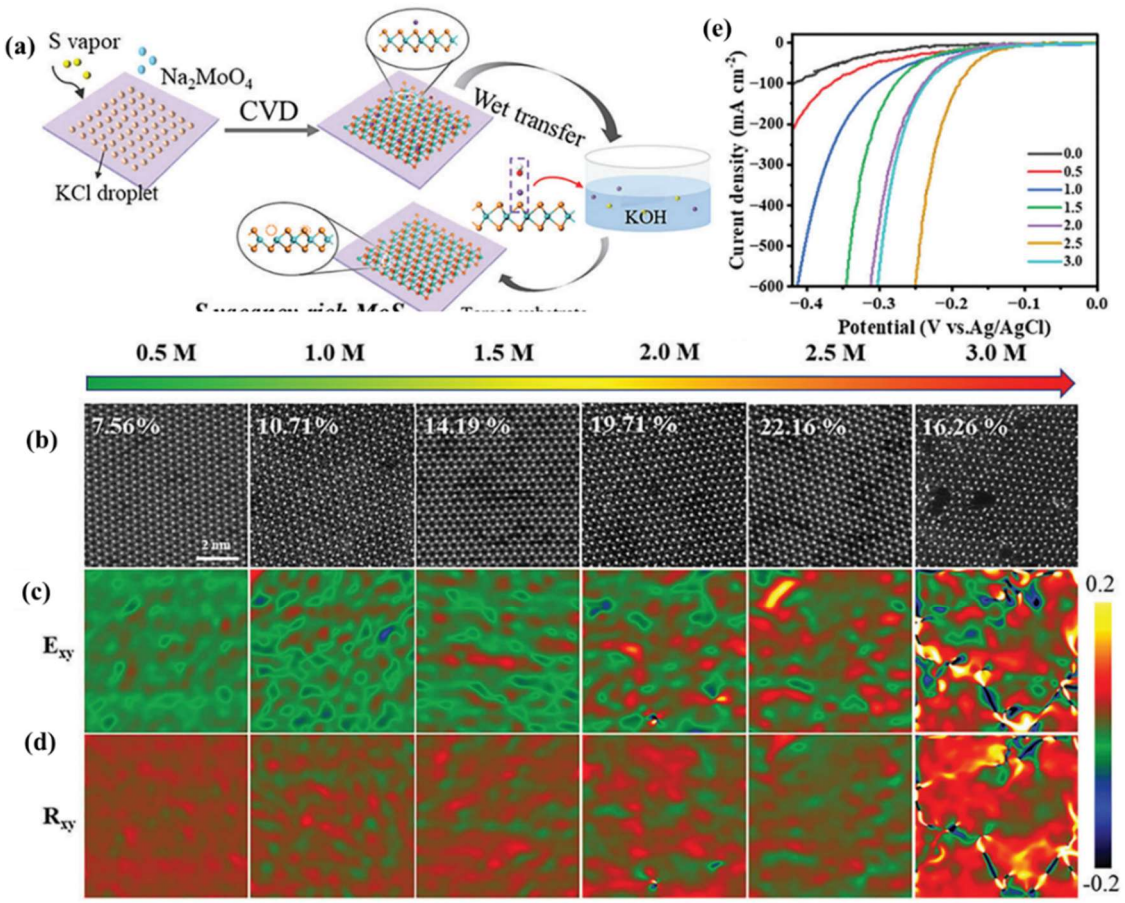

Figure 12. (a) Synthesis process of S-vacancy-rich MoS_2. **(b)** Sulfur vacancy ratios marked on high-resolution STEM images. **(c)** Strain color scale of shear strain (E_{xy}). **(d)** Strain color scale of rotation lattice (rotation-*xy*, or R_{xy}). **(e)** HER performances [79].

In addition, metal or heteroatom doping [18,80–82] has been found to be another efficient way to activate basal planes and increase active sites. For instance, Xiao et al. [80] found that N dopants in MoS_2 exhibited a small overpotential of 35 mV with a low Tafel slope of 41 $mV \cdot dec^{-1}$. The experimental and first-principle approach confirmed that N dopants activated S-edge sites and enhanced the conductivity of MoS_2. Fu et al. [18] used metal Zn to produce S vacancies on MoS_2 via Zn doping, as well as to activate the basal planes. The obtained MoS_2 had a decreased ΔG_H on S vacancy sites of MoS_2 near Zn atoms, which contributed to a low HER overpotential of 194 mV at 10 $mA \cdot cm^{-2}$. Anjum et al. [83] prepared an all-in-one MoS_2 electrocatalyst with NH_3 molecules intercalation (ammoniated MoS_2, or A-MoS_2). Subsequently, the A-MoS_2 was in-situ reduced to remove the intercalated NH_3 and H_2S and to form all-in-one MoS_2 with multifunctional active sites (R-MoS_2). The electrocatalytic HER performance of the R-MoS_2 was even superior to that of commercial Pt/C, indicating its high potential for HER systems.

4.2.2. Phase regulation

As we know, MoS_2 has three different phase structures, which are 1T, 2H and 3R. 2H-MoS_2 has been widely researched as an electrocatalyst. Recently, a considerable amount of works in the literature revealed that 1T-MoS_2 exhibited an enhanced catalytic HER activity than 2H-MoS_2 due to its high conductivity and unique structural advantage. Lukowski et al. [84] reported the fabrication of 1T-MoS_2 nanosheets using chemical exfoliation, which showed superior catalytic HER activity, attributing to favorable reaction kinetics, good conductivity and increased density of active sites. Yin et al. [85] systematically explored the correlation among the phase structure, edge sites, S vacancies and catalytic HER activity. They synthesized porous 1T-MoS_2 (P-1T-MoS_2) via lithiation, desulfurization and exfoliation (**Figure 13(a–d)**; steps I, II and III) and porous 2H-MoS_2 nanosheets (P-2H-MoS_2, **Figure 13(e)**) via facile annealing from the synthesized P-1T-MoS_2 (Step IV). The porous feature of P-1T-MoS_2 was confirmed via TEM, as indicated by red arrows in **Figure 13(f)**. **Figure 13(g)** shows the linear sweep voltammetry (LSV) curves, in which P-1T-MoS_2 displayed a much higher HER performance with 153 mV at $j = -10$ $mA \cdot cm^{-2}$ than other types of MoS_2. The results revealed that the HER performance of 1T-MoS_2 generally was superior to that of 2H-MoS_2, indicating that the phase played a crucial role in catalytic HER. In addition, both edge sites and S vacancies also enhanced the catalytic HER property. This study offers a reference for developing highly active MoS_2 electrocatalysts.

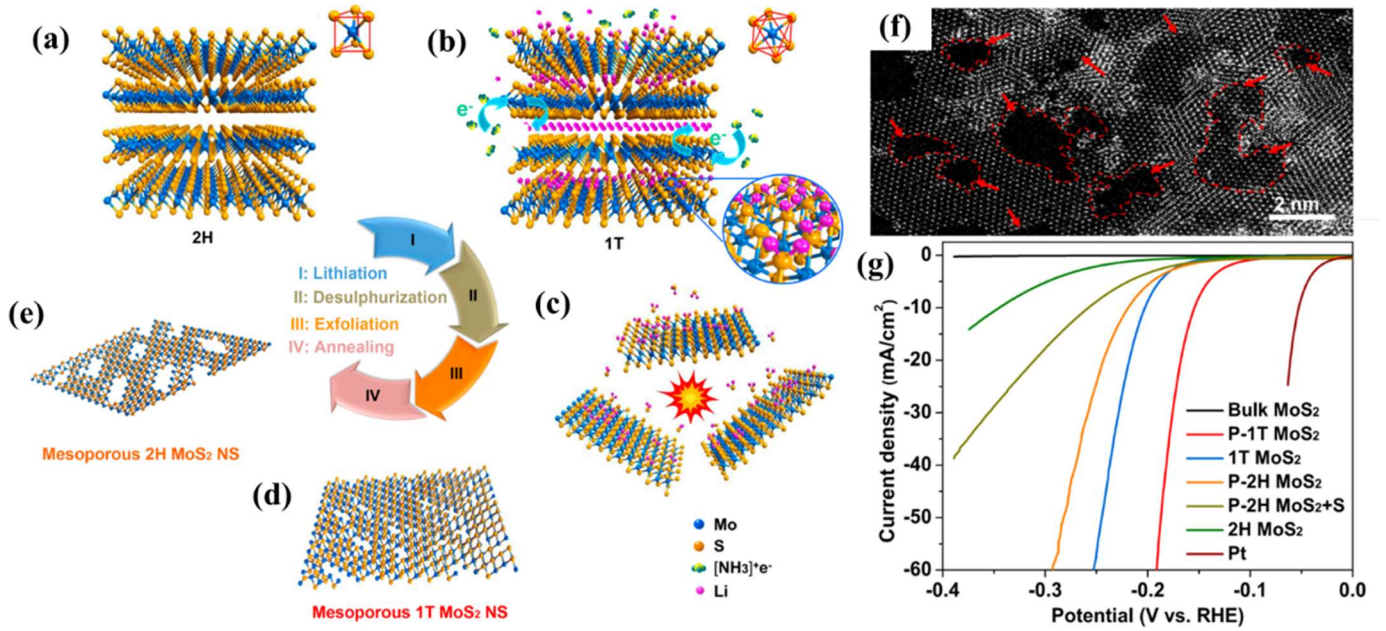

Figure 13. Schematic illustration of preparation of mesoporous 1T-MoS_2 nanosheets from bulk MoS_2 via **(a)** lithiation **(b)**, desulfurization and **(c)** exfoliation. **(d)** P-1T-MoS_2 from Steps I, II and III. **(e)** P-2H-MoS_2 from Step IV. **(f)** TEM image of 1T-MoS_2. **(g)** Catalytic activities of samples [85].

For facile and controllable preparation of 1T-MoS_2, numerous studies have been devoted to developing efficient synthesis methods. Chang's group [86] accurately fabricated the different phases of MoS_2 by using Li-molten salt and tuning the calcination temperature via exfoliation. The obtained monolayer 1T-MoS_2 was found to directly rely on annealing temperature and had excellent catalytic HER activity. Zhu et al. [87] reported a scalable phase-engineering strategy to obtain monolayer 1T-MoS_2 using weak Ar-plasma bombardment. The existence of S vacancies (point defects) was found to stabilize the 1T-MoS_2 phase. Liu et al. [88] developed a simple hydrothermal route to prepare 1T-MoS_2 nanosheet arrays vertically grown on a carbon cloth (1T-MoS_2/CC), which was stable for 45 days under ambient conditions. The obtained 1T-MoS_2/CC provided rich active sites, enhanced accessibility and good conductivity, leading to an attractive HER activity with 151 mV to reach 10 $mA \cdot cm^{-2}$. Besides, Li et al. [89] synthesized defect-rich 1T-MoS_2 via the solvothermal method, where the proportion of the 1T-MoS_2 was tuned using the amount of acetic acid. The optimized 1T-MoS_2 delivered a low overpotential of 136 mV at 10 $mA \cdot cm^{-2}$ and a small Tafel slope of 45 $mV \cdot dec^{-1}$. Yang's group [90] reported a large-scale strategy for high-concentration 1T-MoS_2 with an excellent HER performance via ionic-liquid-assisted hydrothermal reaction, which can be extended to prepare 1T-WS_2, 1T-$MoSe_2$ and 1T-WSe_2.

Although many synthesis methods have been proposed, the thermodynamic metastability of 1T-MoS_2 extensively limits its stability. Recently, atom intercalation in MoS_2 has been confirmed to stabilize MoS_2's phase structure. For instance, Ekspong et al. [91] developed sulfur-rich intercalated 1T-MoS_2 on graphitic nanoribbons with an S:Mo ratio of ~2.3:1, which sustained its stability for several months. Both experimental and theoretical results found that the active sites on the basal planes were activated with an outstanding ΔG_H value of 0.06 eV, which in turn improved catalytic

activity. Gao's group [92] confirmed that the formation of 1T-MoS_2 can be induced using metal doping. Their results found that Co/Ni co-doping provided abundant electrons for Mo atoms, subsequently leading to phase transition. The obtained Co/Ni-MoS_2 possessed an excellent alkaline HER property. Jiang et al. [93] proposed a strategy of Se and O co-insertion to induce the transition of MoS_2 from the 2H phase to the 1T phase. Guo's group [94] reported a chemical etching method to construct 1T-MoS_2 with different S vacancies (1T-MoS_2-V_S) for efficient catalytic HER. **Figure 14(a)** shows the schematic of the synthesis of 1T-MoS_2-V_S. K^+ ions intercalated in the interlayer of 2H-MoS_2 to form $KMoS_2$, and 1T-MoS_2 was obtained by the extraction of K^+ from $KMoS_2$. Afterward, the 1T-MoS_2 was immersed in an acidic $K_2Cr_2O_7$ solution to obtain S vacancies. The electrochemical measurements are shown in **Figure 14(b–d)**. The 1T-MoS_2-V_S exhibited a lower overpotential of 158 mV at 10 $mA \cdot cm^{-2}$ and a smaller Tafel slope of 74.5 $mV \cdot dec^{-1}$. A little degradation in its current density after a continuous 24-h test suggested remarkable stability for HER. Particularly, the electronic states of the 1T-MoS_2-V_S (**Figure 14(e–g)**) demonstrated the charge redistribution with the activated Mo-Mo bonds, which led to an optimal ΔG_{H^*} value for catalytic HER.

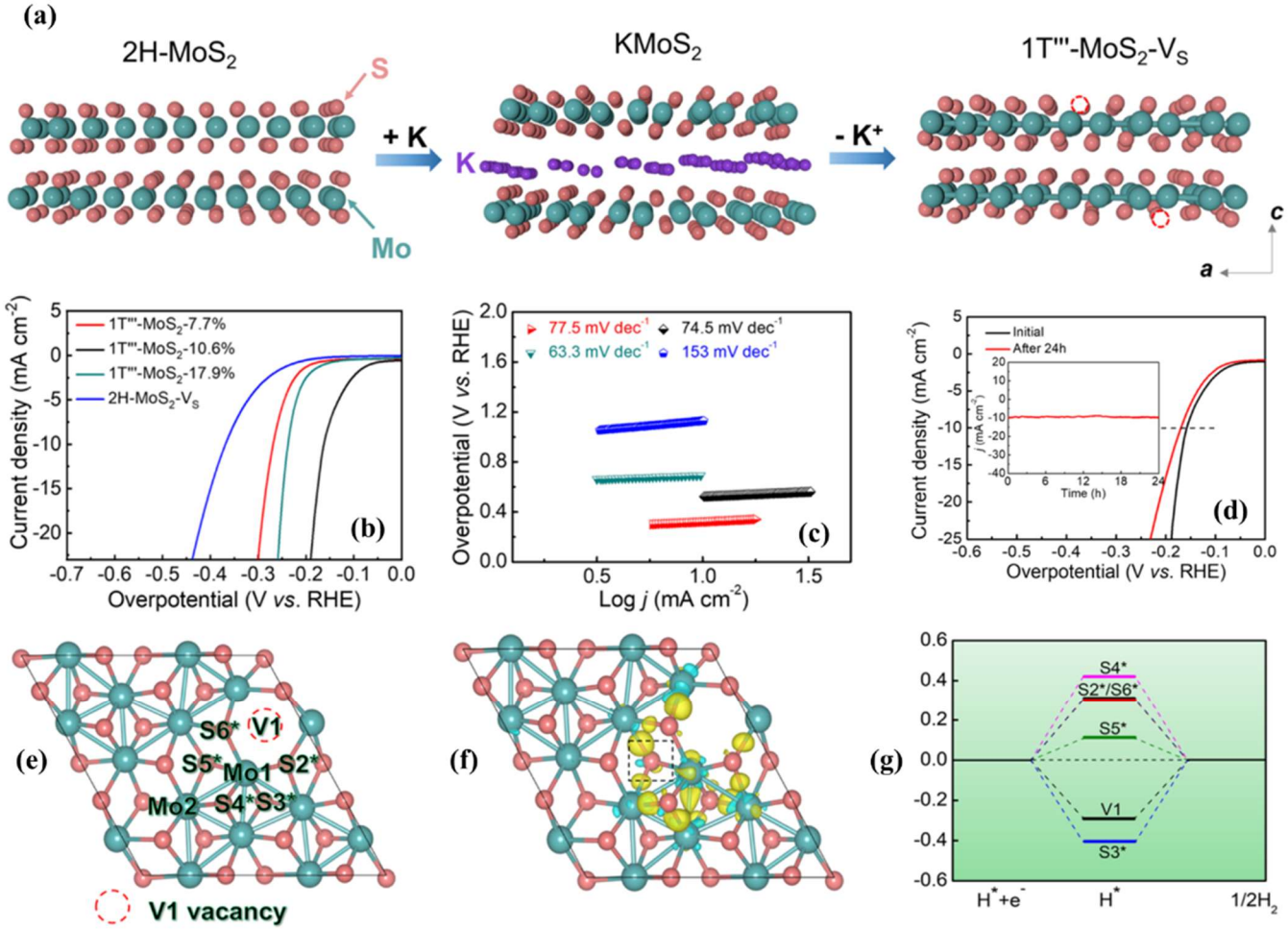

Figure 14. (a) Fabrication procedure of 1T-MoS_2-V_S. **(b)** LSV curves of 1T-MoS_2-V_S. **(c)** Tafel slope of 1T-MoS_2-V_S. **(d)** Stability result of 1T-MoS_2-V_S. **(e)** Optimized structure, **(f)** Calculated charge density difference. **(g)** ΔG_{H^*} in different exposed S atoms of 1T-MoS_2-V_S [94].

4.2.3. Heterostructure construction

Recently, heterostructure construction has been shown to demonstrate outstanding performance for electrocatalysis, including electrocatalytic HER, OER, etc. Usually, heterostructured catalysts are composed of two/multiple functional components with tunable electronic interaction and distinct synergetic effects. Herein, MoS_2 heterostructured electrocatalysts for HER are summarized. A MoS_2−Ni_3S_2 heterostructure was reported by Yang's group [95] which was directly supported by Ni foam. MoS_2 nanosheets were hierarchically decorated on Ni_3S_2 nanorods, in which the hierarchical MoS_2-Ni_3S_2 heterostructure showed highly active heterointerfaces and facilitated charge transport, thus presenting a low overpotential of 98 mV to reach 10 $mA \cdot cm^{-2}$. A Ni_2P/MoS_2 heterostructure is constructed by Kim et al. [96] which were hybridized with conductive N-doped carbon supports. The generated electrocatalyst delivered Pt-like catalytic HER activity. N-doped carbon played a key role in the conductivity and stability of the Ni_2P/MoS_2 heterostructure, enhancing the potential for hydrogen production. Kim et al. [97] developed a 0D–2D Co_9S_8–MoS_2 heterostructure, where ultrasmall Co_9S_8 nanoparticles were loaded on the surface of MoS_2 using Co-S-Mo covalent bonds. The Co_9S_8–MoS_2 heterostructure offered electron-rich Mo sites generated by the interface charge redistribution from Co to Mo sites. Furthermore, S defects, which were formed due to reductive annealing, activated adjacent Mo atoms to increase catalytic HER. The experimental and DFT results revealed that the 0D–2D Co_9S_8–MoS_2 heterostructure presented an excellent catalytic HER activity in electrolytes with a wide range of pH.

As mentioned above, 1T-MoS_2 has much higher electrical conductivity and a better catalytic HER performance than those of 2H-MoS_2. Wang et al. [98] proposed constructing 1T–2H-MoS_2 heterostructures via a simple one-pot annealing treatment, which showed improved electrical conductivity, had more active sites and delivered promoted electrocatalytic HER properties. Cheng et al. [99] constructed a MoS_2/α-MoC heterostructure using two straightforward and facile steps, as shown in **Figure 15(a)**, which formed an in-plane heterostructure of MoS_2(002)/α-MoC(111) (**Figure 15(b)**). The MoS_2/α-MoC led to lattice strain with an adjustive electronic configuration and thus presented Pt-like activity for HER with only a low 78 mV of overpotential at 10 $mA \cdot cm^{-2}$ and a small Tafel slope of 38.7 $mV \cdot dec^{-1}$ (**Figure 15(c,d)**). Besides, Sun et al. [100] developed Mo-MoS_2 Mott-Schottky heterojunctions (Mo-MoS_2 MSH) by combining the semiconductor MoS_2 with the metal Mo. The electronic structure of the Mo-MoS_2 MSH was effectively optimized with enhanced H adsorption. The Mo-MoS_2 MSH only needed overpotentials of 91, 138 and 128 mV to achieve 10 $mA \cdot cm^{-2}$ in acid, alkaline and neutral solution, respectively.

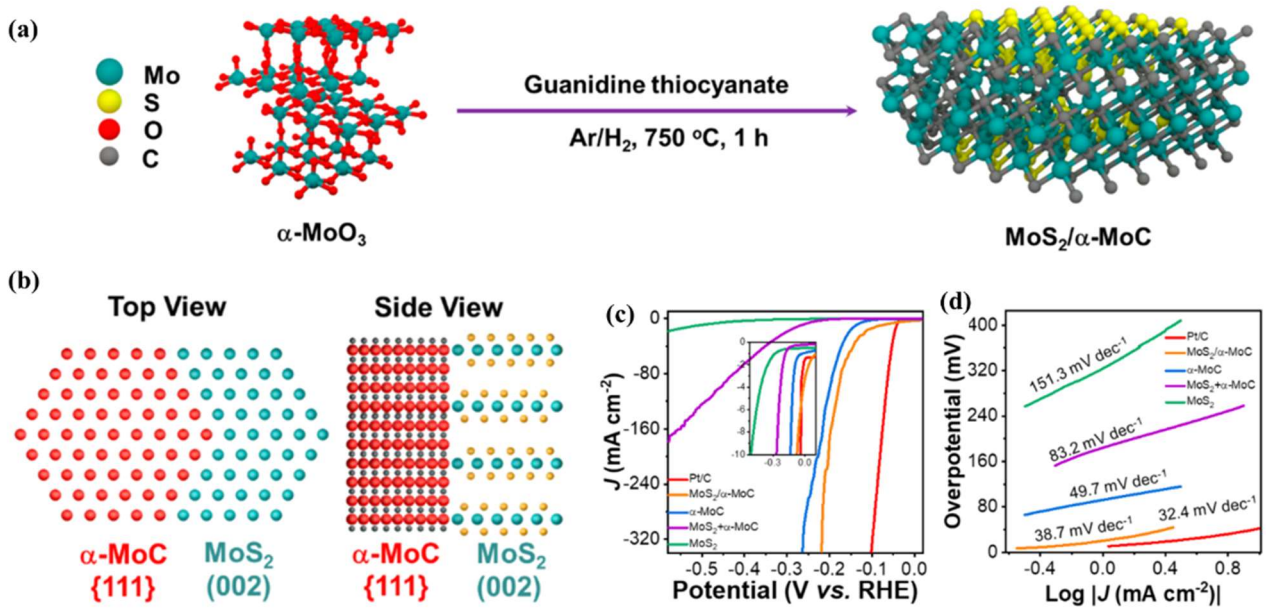

Figure 15. (a) Schematic illustration of synthesis of MoS_2/α-MoC heterostructure. **(b)** Hypothesized top and side views of in-plane structure. **(c)** Polarization curves. **(d)** Tafel slopes [99].

4.2.4. Defect/vacancy engineering

Defect/vacancy engineering is an efficient strategy to construct specific unsaturated active centers and tune electronic structures. Unsaturated active centers can serve as active sites for intermediate adsorption/desorption, thereby enhancing catalytic properties. S-vacancy and Mo-vacancy engineering have been widely confirmed as efficient methods to expose more active sites in MoS_2 and improve HER [101–104]. Generally, S vacancies are more easily formed during the synthesis process. Ye et al. [105] reported the defect engineering of monolayer MoS_2 using O plasma annealing, which resulted in improved HER performance. They illustrated the correlation between changes in MoS_2's microscale structure and HER properties for the first time, proving that defect engineering could produce more catalytic active edge sites and thus promote HER activity. Li et al. [101] also explored the relationship between HER activity and surface S vacancies of MoS_2. With the increase in S vacancies, two different domains were reported, which were point defects at low S-vacancy concentrations and a large number of undercoordinated Mo atoms at high S-vacancy concentrations. The HER activity rapidly accelerated by the point defects, but the highest HER performance was obtained from the formation of undercoordinated Mo atoms through S stripping. This work provides a reference for the development of defected MoS_2 to boost HER. Wang's group [104] initially regulated the state (concentration and distribution) of S vacancies via high throughput calculations. The state of S vacancies was experimentally modulated using etching parameters (etching duration, etching temperature and etching solution concentration). The results found that MoS_2 with single S vacancies exhibited optimal HER performance than that of MoS_2 with agglomerate S vacancies. The outstanding property can be attributed to the more effective adjustment of the surface electronic structure and electrical transportation.

Zhan et al. [106] explored the relationship between the local atomic environment of vacancies and HER performance of MoS_2. A series of models with different vacancies were first built to theoretically evaluate ΔG_{H^*}. The calculation results confirmed that H* can be adsorbed on Mo atoms and that ΔG_{H^*} decreased due to the existence of vacancies. Among these models, M-MoS_2 (V_{MoS_5}-MoS_2) with more Mo-terminated vacancies had the lowest ΔG_{H^*} of 0.04 eV. Generally, ΔG_{H^*} was found to rely on the interfacial electronic structure. As shown in **Figure 16(a)**, exposed Mo atoms in M-MoS_2 can obtain more electrons to increase the electron density of Mo atoms, which can be verified via the Bader charge (**Figure 16(b)**). The average Bader charge of Mo atoms in M-MoS_2 was ~5.20, which was higher than those of MoS_2 (perfect MoS_2) and S-MoS_2 (V_{MoS_2}-MoS_2). Electron-rich Mo atoms contributed to the Volmer reaction for HER. Additionally, the larger electron cloud (**Figure 16(c)**) on Mo sites in M-MoS_2 produced a stronger electronic coupling and more efficient orbital interaction (**Figure 16(d)**) for more favorable H desorption. Specifically, the calculation of integrated crystal orbital Hamilton populations (ICOHPs) resulted in more negative values, as shown in **Figure 16(e)**, which further revealed enhanced H desorption. The ICOHP values of MoS_2, M-MoS_2 and S-MoS_2 were −0.06, −2.20 and −2.35, respectively. M-MoS_2 possessed a moderate ICOHP value, suggesting beneficial H adsorption. These results showed that the atomic environment surrounding vacancies was crucial for effectively regulating the Volmer step and H adsorption. MoS_2 with more Mo terminated vacancies was favorable for better HER performance. As seen from LSV curves in **Figure 16(f)**, MoS_2 with the fewest vacancies had the largest overpotential of 277 mV at 10 $mA \cdot cm^{-2}$ (η_{10}). The overpotential for S-MoS_2 decreased to 235 mV. M-MoS_2 was identified as the optimal sample for HER with the smallest η_{10} value of 210 mV. In particular, along with an overpotential of 250 mV, M-MoS_2 showed a current density of 51.4 $mA \cdot cm^{-2}$, which was about four-fold that of S-MoS_2 and eight-fold that of MoS_2. The Tafel plots in **Figure 16(g)** show slopes of 60.7, 110.1 and 125.8 $mV \cdot dec^{-1}$ for M-MoS_2, S-MoS_2 and MoS_2, respectively, where a lower Tafel slope represents better HER kinetics. As shown in **Figure 16(h)**, M-MoS_2 remained almost unchanged for 40 h to generate H_2. This work provides a more profound understanding of defect engineering for the design of highly active catalysts.

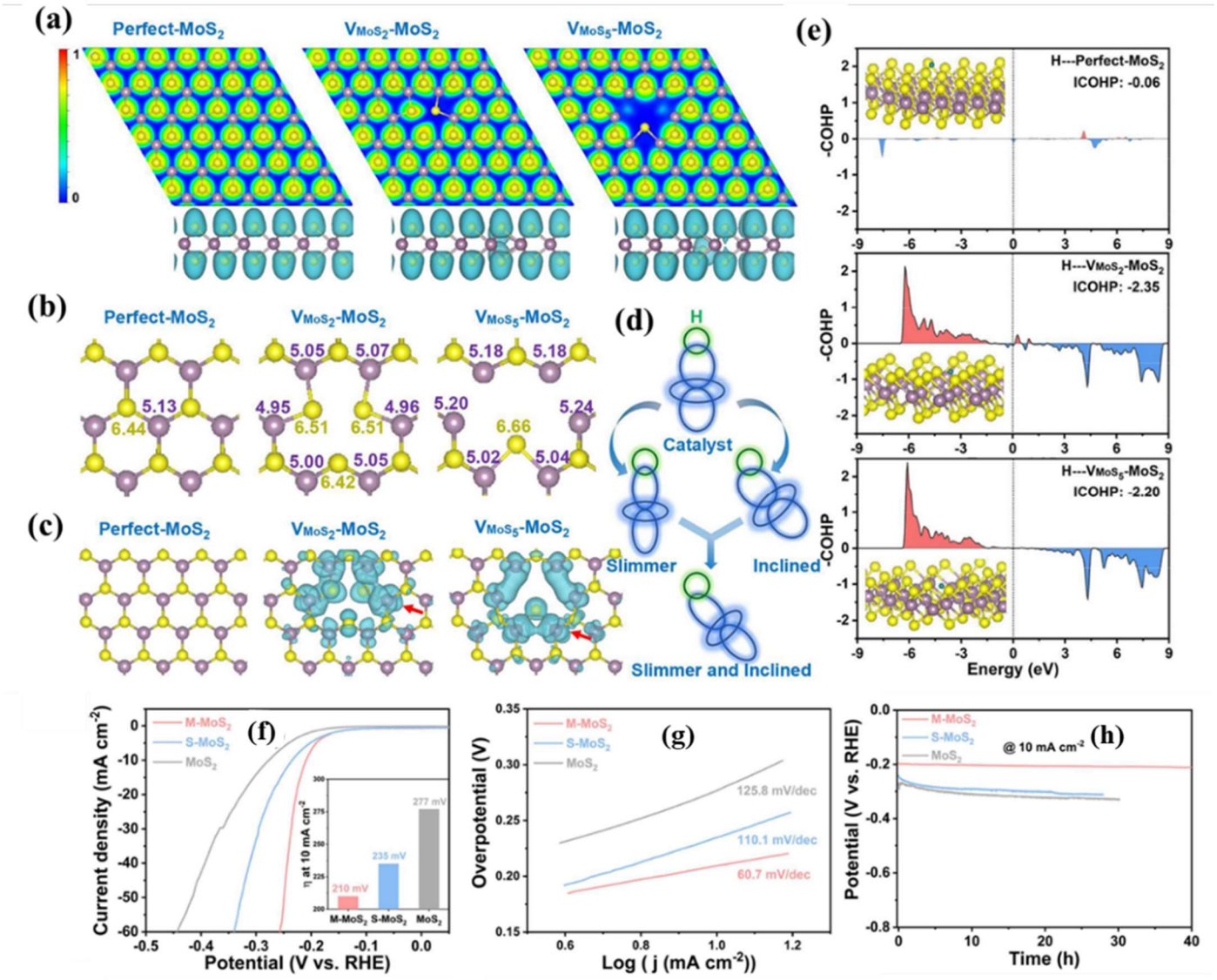

Figure 16. (a) Top view of (001) planes and side view of electron localization function maps. **(b)** Bader charges of atoms around vacancy in MoS_2 (perfect MoS_2), S-MoS_2 (V_{MoS_2}-MoS_2) and M-MoS_2 (V_{MoS_5}-MoS_2). **(c)** Unoccupied orbital distribution near Fermi level of MoS_2, S-MoS_2 and M-MoS_2 (red arrow denotes H-adsorption site). **(d)** Schematic diagram of orbital interaction under different conditions. **(e)** ICOHP values of H adsorption on MoS_2, S-MoS_2 and M-MoS_2 (bonding and antibonding states in ICOHP are depicted in red and blue, respectively). **(f)** Linear sweep voltammetry (LSV) curves in 0.5M H_2SO_4 with scan rate of 5 $mV \cdot s^{-1}$ (inset: overpotential values at 10 $mA \cdot cm^{-2}$). **(g)** Tafel slopes. **(h)** Long-term stability [106].

Mo-vacancy engineering has also been considered as a good method to improve metal sulfides for energy storage and conversion [107–109] and especially for electrocatalysis. Ge et al. [108] developed abundant Mo vacancies in a MoS_2-based composite. Experimental and theoretical calculations revealed that Mo vacancies modulated the electronic structure of S sites to regulate the free energy of H adsorption, thus enhancing catalytic HER. Shi et al. [109] reported a Frenkel-defected monolayer MoS_2 catalyst, in which S and Mo vacancies co-existed in MoS_2 to generate charge distributions. The obtained Frenkel-defected MoS_2 exhibited an outstanding HER activity with a low overpotential of 164 mV.

4.2.5. Element doping

In electrocatalysis, element doping has been deemed to be an effective method to regulate active sites of catalysts for various reactions. Element doping comprises two types: metal doping and heteroatom doping (nonmetal doping). Metal doping (e.g., Zn, Co, Ni, etc.) [110–113] can effectively adjust the electronic structure of Mo sites in MoS_2 to promote high HER performance. For instance, Xu et al. [110] proposed transition metal Zn doping of MoS_2 to engineer its energy level for efficient HER. They found that Zn doping provided an energy level matching the HER's kinetic acceleration, resulting in a superior electrochemical HER activity. Xue et al. [112] developed ultra-small Ni-doped MoS_2 nanosheets on hollow carbon microtubes. The results confirmed that moderate Ni doping tuned the electronic structure of active sites in MoS_2. As a result, the obtained catalyst exhibited excellent activity with enhanced HER kinetics, requiring a low overpotential of 88 mV at 10 $mA \cdot cm^{-2}$ and demonstrating better stability in 0.5M H_2SO_4. Kong et al. [114] used rare earth Ce for a doping strategy to prepare Ce-doped MoS_2. The Ce-doped MoS_2 was rich in defects and regulated the electronic structure, further promoting HER performance with a small overpotential of 113.78 mV.

Heteroatom doping (N, F, P, etc.) [115–119] for enhancing catalytic HER has also received great attention. Li et al. reported N-doped MoS_2, fabricated via a simple one-step hydrothermal strategy, as an efficient HER catalyst [115]. The N doping produced rich S defects to expose Mo sites and adjust the electron density of S atoms to activate S atoms as active sites. The N-doped MoS_2 revealed a much lower overpotential of 168 mV at 10 $mA \cdot cm^{-2}$ than that of pure MoS_2. Zhang et al. [118] developed F-doped MoS_2 with controllable active sites by using a plasma etching strategy. F atoms possess larger electronegativity than S atoms, thus leading to more moderate-free-energy carriers for H* intermediates and delivering five-fold activity enhancement for HER. Shi et al. [119] constructed P-doped 2H-MoS_2 nanoflowers with a crystalline-amorphous heterostructure via a simple calcination method. Rich S vacancies were generated from the P doping. Benefiting from P doping, the crystalline-amorphous heterostructure and S vacancies, the P-doped 2H-MoS_2 demonstrated pH-universal HER activity and excellent stability.

4.2.6. Compound construction by coupling with conductive materials

Although MoS_2 has been regarded as a promising HER electrocatalyst, its low number of active edge sites and its semiconductor feature result in a relatively low activity toward HER. Compound construction by coupling MoS_2 with conductive graphene [120,121], carbon nanotube [122,123], graphdiyne [124,125], etc., has also been reported as a good method to improve HER performance. The unique synergistic effect can be generated to modulate MoS_2 for efficient HER. A rational design of MoS_2-based compounds can adjust the conductivity and expose the active edge sites of MoS_2 [124,126,127]. Li et al. [120] synthesized MoS_2@reduced graphene oxide (RGO) as a highly active HER electrocatalyst. The unique synergistic effect between MoS_2 with RGO enhanced the HER activity with a small overpotential of 64 mV at 10 $mA \cdot cm^{-2}$. Wu et al. [128] reported hierarchical MoS_2/Ti_3C_2-MXene@C compounds with a good catalytic HER. The results revealed that the MoS_2/Ti_3C_2-MXene@C showed greatly improved electrical conductivity and structural stability.

The synergy of compounds also promotes the HER kinetics of MoS_2, thus leading to an outstanding HER performance. Graphdiyne, with its unique atomic arrangement, good conductivity and abundant natural pore structure, has attracted great attention. Hui's group [125] reported a simple strategy to synthesize graphdiyne-encapsulated MoS_2 nanosheets on carbon fiber (GDY-MoS_2 NS/CF), as shown in **Figure 17(a–c)**. It can be clearly seen in **Figure 17(d)** that the GDY-MoS2 NS/CF had the best catalytic activity among all catalysts, exhibiting a high current density (J) at the low overpotential (η). The experimental and theoretical calculations verified that graphdiyne on the surface of MoS_2 induced a phase transformation from 2H-MoS_2 to 1T-MoS_2 and decreased the free energy for H adsorption (**Figures 17(e,f)**). Song et al. [126] found that the construction of MoS_2@carbon quantum dots (CQDs) enabled hydrogen spillover to accelerate HER activity. The CQDs on the surface of MoS_2 led to charge redistribution and electrons gradually transferring from C sites in the CQDs to S sites in MoS_2, promoting hydrogen spillover.

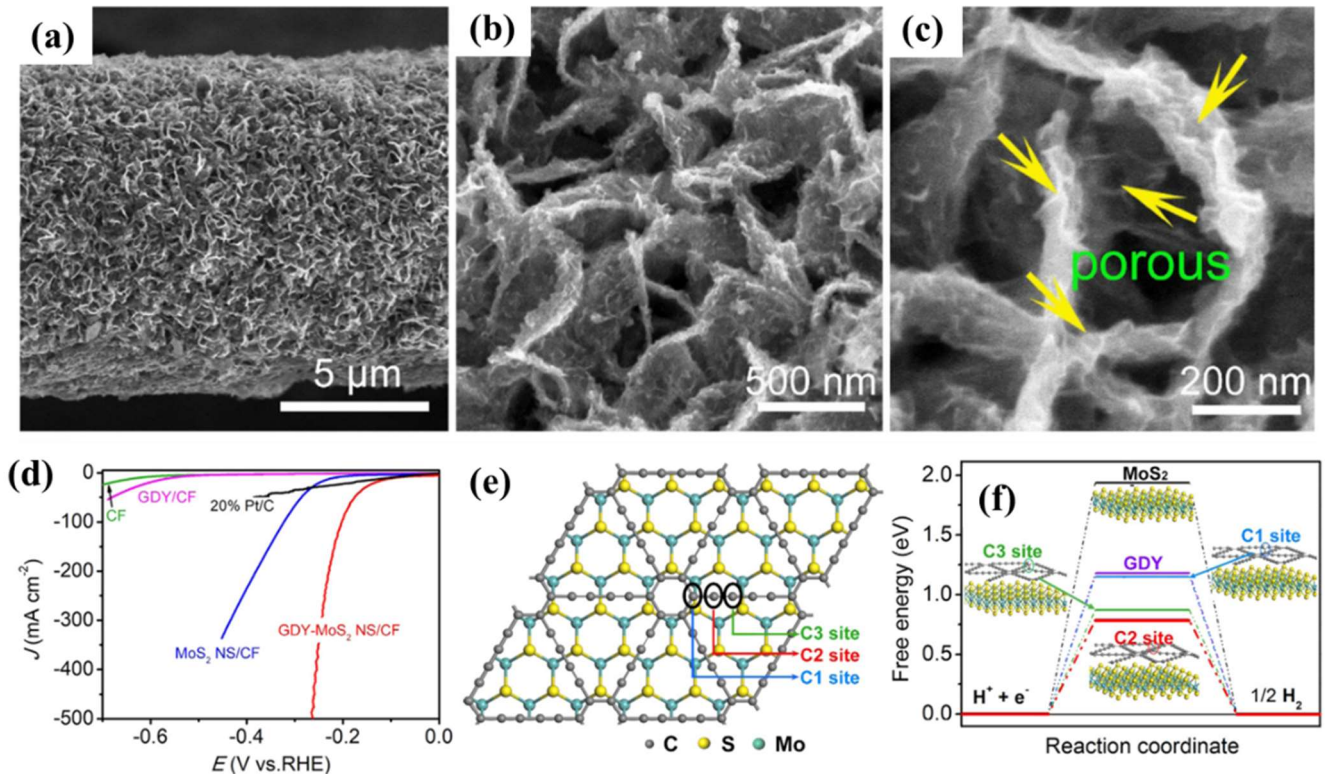

Figure 17. (a–c) SEM images of GDY-MoS_2 NS/CF. **(d)** LSV curves in alkaline solution. **(e)** Top view of optimized structure of GDY-MoS_2. **(f)** Free energy diagram of HER [125].

5. Conclusion and prospects

This review summarized the recent progress and improved strategies of MoS_2 for photocatalytic HER and electrocatalytic HER. For photocatalytic HER, many novel strategies have been proposed to enhance the photocatalytic activity of MoS_2, such as surface engineering, heterostructure construction and defect engineering. These approaches have led to significant improvements in the efficiency of MoS_2-based photocatalysts. In addition, considerable efforts have also focused on improving the light absorption range of MoS_2 photocatalysts through bandgap engineering and

doping with heteroatoms, which allow for more efficient utilization of solar energy for photocatalytic reactions. Some new synthesis methods and surface passivation techniques have also been found to decrease the photo-corrosion of MoS_2 under light conditions and promote long-term performance. Also, there has been significant progress in MoS_2 as an electrocatalyst in electrocatalytic hydrogen production. The edge sites of MoS_2 serve as active sites for catalytic HER, and MoS_2 exhibits high catalytic HER activity under both acidic and alkaline conditions. The electronic structure of MoS_2 can be manipulated via morphology tuning, element doping, nanostructure design, heterostructure construction and chemical composition construction to accelerate its electrocatalytic HER activity.

Overall, although recent research works on MoS_2 for photo/electrocatalysis have effectively enhanced its HER activity, which is even close to those of many advanced HER catalysts, there are still some issues during photo/electrocatalysis. New sustainable synthesis methods for MoS_2 should be developed to minimize the use of toxic precursors and energy-intensive processes, which can contribute to the large-scale preparation of MoS_2 catalysts. Efforts should be devoted to enhancing the catalytic activity of MoS_2 catalysts for HER. Specially, the electrocatalytic HER performance of MoS_2 catalysts still lags behind those of commercial Pt-based catalysts. It is urgent to further investigate the fundamental catalytic mechanisms of MoS_2 for HER through operando characterization techniques and theoretical modeling, which can provide insights into the structure-property relationships and guide the rational design of the catalysts. In addition, practical applications require catalysts with excellent long-term stability and strong corrosion resistance, i.e., not limited to only tens of hours in the laboratory. Despite the efficient utilization of 2D MoS_2 for electrocatalysis and photocatalysis, enormous challenges remain, and ongoing research is expected to make significant progress soon.

Funding: This work was supported by the National Natural Science Foundation of China (Grant No. 22202042 and No. 22308070), the Guangdong Basic and Applied Basic Research Foundation (Grant No. 2022A1515140012), the Yunnan Fundamental Research Projects (Grant No. 202401CF070036), and the China Postdoctoral Science Foundation (Grant No. 2023M740794).

Conflict of interest: The authors declare no conflict of interest.

References

1. Li R, Kuang P, Wageh S, et al. Potential-dependent reconstruction of Ni-based cuboid arrays for highly efficient hydrogen evolution coupled with electro-oxidation of organic compound. Chemical Engineering Journal. 2023; 453: 139797. doi: 10.1016/j.cej.2022.139797
2. Lu G, Wang Z, Bhatti UH, et al. Recent progress in carbon dioxide capture technologies: A review. Clean Energy Science and Technology. 2023; 1(1). doi: 10.18686/cest.v1i1.32
3. Jiehui Z, Su Y, Wang W, et al. Hydrogen-electricity coupling energy storage systems: Models, applications, and deep reinforcement learning algorithms. Clean Energy Science and Technology. 2024; 2(1): 96. doi: 10.18686/cest.v2i1.96
4. Zhang Y, Xiao Y, Abuelgasim S, et al. A brief review of hydrogen production technologies. Clean Energy Science and Technology. 2024; 2(1): 117. doi: 10.18686/cest.v2i1.117
5. Gu X, Lin S, Qi K, et al. Application of tungsten oxide and its composites in photocatalysis. Separation and Purification Technology. 2024; 345: 127299. doi: 10.1016/j.seppur.2024.127299

6. Qureshi F, Yusuf M, Pasha AA, et al. Sustainable and energy efficient hydrogen production via glycerol reforming techniques: A review. International Journal of Hydrogen Energy. 2022; 47(98): 41397-41420. doi: 10.1016/j.ijhydene.2022.04.010
7. Chen J, Cao J, Zhou J, et al. Mechanism of highly enhanced hydrogen storage by two-dimensional 1T′ MoS_2. Physical Chemistry Chemical Physics. 2020; 22(2): 430-436. doi: 10.1039/c9cp04402g
8. Qi K, Zhuang C, Zhang M, et al. Sonochemical synthesis of photocatalysts and their applications. Journal of Materials Science & Technology. 2022; 123: 243-256. doi: 10.1016/j.jmst.2022.02.019
9. Zhang J, Bifulco A, Amato P, et al. Copper indium sulfide quantum dots in photocatalysis. Journal of Colloid and Interface Science. 2023; 638: 193-219. doi: 10.1016/j.jcis.2023.01.107
10. Zhang J, Zhao Y, Qi K, et al. $CuInS_2$ quantum-dot-modified g-C_3N_4 S-scheme heterojunction photocatalyst for hydrogen production and tetracycline degradation. Journal of Materials Science & Technology. 2024; 172: 145-155. doi: 10.1016/j.jmst.2023.06.042
11. Pan J, Shen S, Chen L, et al. Core–Shell Photoanodes for Photoelectrochemical Water Oxidation. Advanced Functional Materials. 2021; 31(36). doi: 10.1002/adfm.202104269
12. Pan J, Wang B, Wang J, et al. Activity and Stability Boosting of an Oxygen-Vacancy-Rich $BiVO_4$ Photoanode by NiFe-MOFs Thin Layer for Water Oxidation. Angewandte Chemie International Edition. 2020; 60(3): 1433-1440. doi: 10.1002/anie.202012550
13. Pan J, Wang B, Shen S, et al. Introducing Bidirectional Axial Coordination into $BiVO_4$@Metal Phthalocyanine Core–Shell Photoanodes for Efficient Water Oxidation. Angewandte Chemie International Edition. 2023; 62(38). doi: 10.1002/anie.202307246
14. Yang R, Fan Y, Zhang Y, et al. 2D Transition Metal Dichalcogenides for Photocatalysis. Angewandte Chemie International Edition. 2023; 62(13). doi: 10.1002/anie.202218016
15. Li Q, Huang L, Dai W, et al. Controlling 1T/2H heterophase junctions in the MoS_2 microsphere for the highly efficient photocatalytic hydrogen evolution. Catalysis Science & Technology. 2021; 11(24): 7914-7921. doi: 10.1039/d1cy01340h
16. Kuc A, Heine T. The electronic structure calculations of two-dimensional transition-metal dichalcogenides in the presence of external electric and magnetic fields. Chemical Society Reviews. 2015; 44(9): 2603-2614. doi: 10.1039/c4cs00276h
17. Li Y, Zhang Y, Tong X, et al. Recent progress on the phase modulation of molybdenum disulphide/diselenide and their applications in electrocatalysis. Journal of Materials Chemistry A. 2021; 9(3): 1418-1428. doi: 10.1039/d0ta08514f
18. Fu Q, Han J, Wang X, et al. 2D Transition Metal Dichalcogenides: Design, Modulation, and Challenges in Electrocatalysis. Advanced Materials. 2020; 33(6). doi: 10.1002/adma.201907818
19. Wu W, Niu C, Wei C, et al. Activation of MoS_2 Basal Planes for Hydrogen Evolution by Zinc. Angewandte Chemie International Edition. 2019; 58(7): 2029-2033. doi: 10.1002/anie.201812475
20. Liang Z, Xue Y, Wang X, et al. Co doped MoS_2 as cocatalyst considerably improved photocatalytic hydrogen evolution of g-C_3N_4 in an alkalescent environment. Chemical Engineering Journal. 2021; 421: 130016. doi: 10.1016/j.cej.2021.130016
21. Mohan M, Shetti NP, Aminabhavi TM. Phase dependent performance of MoS_2 for supercapacitor applications. Journal of Energy Storage. 2023; 58: 106321. doi: 10.1016/j.est.2022.106321
22. Fujishima A, Honda K. Electrochemical Photolysis of Water at a Semiconductor Electrode. Nature. 1972; 238(5358): 37-38. doi: 10.1038/238037a0
23. Chen F, Zhang Y, Huang H. Layered photocatalytic nanomaterials for environmental applications. Chinese Chemical Letters. 2023; 34(3): 107523. doi: 10.1016/j.cclet.2022.05.037
24. Cheng XM, Zhao J, Sun WY. Facet-Engineering of Materials for Photocatalytic Application: Status and Future Prospects. EnergyChem. 2022; 4(5): 100084. doi: 10.1016/j.enchem.2022.100084
25. Ali SA, Ahmad T. Enhanced hydrogen generation via overall water splitting using novel MoS_2-BN nanoflowers assembled TiO_2 ternary heterostructures. International Journal of Hydrogen Energy. 2023; 48(58): 22044-22059. doi: 10.1016/j.ijhydene.2023.03.118
26. Ma J, Xu L, Yin Z, et al. “One stone four birds” design atom co-sharing BiOBr/Bi_2S_3 S-scheme heterojunction photothermal synergistic enhanced full-spectrum photocatalytic activity. Applied Catalysis B: Environmental. 2024; 344: 123601. doi: 10.1016/j.apcatb.2023.123601
27. Dong X, Xu L, Ma J, et al. Enhanced interfacial charge transfer and photothermal effect via in-situ construction of atom co-sharing Bi plasmonic/$Bi_4O_5Br_2$ nanosheet heterojunction towards improved full-spectrum photocatalysis. Chemical Engineering Journal. 2023; 459: 141557. doi: 10.1016/j.cej.2023.141557

28. Li Y, Ma J, Xu L, et al. Enhancement of Charge Separation and NIR Light Harvesting through Construction of 2D–2D $Bi_4O_5I_2$/BiOBr: Yb^{3+}, Er^{3+} Z-Scheme Heterojunctions for Improved Full-Spectrum Photocatalytic Performance. Advanced Science. 2023; 10(13). doi: 10.1002/advs.202207514
29. Kudo A, Miseki Y. Heterogeneous photocatalyst materials for water splitting. Chem Soc Rev. 2009; 38(1): 253-278. doi: 10.1039/b800489g
30. Gao W, Zhang S, Wang G, et al. A review on mechanism, applications and influencing factors of carbon quantum dots based photocatalysis. Ceramics International. 2022; 48(24): 35986-35999. doi: 10.1016/j.ceramint.2022.10.116
31. Zhang C, Li Y, Li M, et al. Continuous photocatalysis via photo-charging and dark-discharging for sustainable environmental remediation: Performance, mechanism, and influencing factors. Journal of Hazardous Materials. 2021; 420: 126607. doi: 10.1016/j.jhazmat.2021.126607
32. Hong M, Shi J, Huan Y, et al. Microscopic insights into the catalytic mechanisms of monolayer MoS2 and its heterostructures in hydrogen evolution reaction. Nano Research. 2019; 12(9): 2140-2149. doi: 10.1007/s12274-019-2370-3
33. Li S, Sun J, Guan J. Strategies to improve electrocatalytic and photocatalytic performance of two-dimensional materials for hydrogen evolution reaction. Chinese Journal of Catalysis. 2021; 42: 511-556. doi:10.1016/S1872-2067(20)63693-2
34. Zong X, Wu G, Yan H, et al. Photocatalytic H2 Evolution on MoS_2/CdS Catalysts under Visible Light Irradiation. The Journal of Physical Chemistry C. 2010; 114(4): 1963-1968. doi: 10.1021/jp904350e
35. Chen J, Wu X, Yin L, et al. One-pot Synthesis of CdS Nanocrystals Hybridized with Single-Layer Transition-Metal Dichalcogenide Nanosheets for Efficient Photocatalytic Hydrogen Evolution. Angewandte Chemie International Edition. 2014; 54(4): 1210-1214. doi: 10.1002/anie.201410172
36. Kang Y, Gong Y, Hu Z, et al. Plasmonic hot electron enhanced MoS_2 photocatalysis in hydrogen evolution. Nanoscale. 2015; 7(10): 4482-4488. doi: 10.1039/c4nr07303g
37. Liu C, Wang L, Tang Y, et al. Vertical single or few-layer MoS_2 nanosheets rooting into TiO_2 nanofibers for highly efficient photocatalytic hydrogen evolution. Applied Catalysis B: Environmental. 2015; 164: 1-9. doi: 10.1016/j.apcatb.2014.08.046
38. Xue Y, Min S, Meng J, et al. Light-induced confined growth of amorphous Co doped MoSx nanodots on TiO_2 nanoparticles for efficient and stable in situ photocatalytic H_2 evolution. International Journal of Hydrogen Energy. 2019; 44(16): 8133-8143. doi: 10.1016/j.ijhydene.2019.02.057
39. Alharthi FA, Hasan I. Visible light-driven efficient photocatalytic hydrogen production using nickel-doped molybdenum disulfide (Ni@MoS_2) nanoflowers. Journal of Materials Science. 2024; 59(8): 3394-3405. doi: 10.1007/s10853-024-09435-5
40. Sorgenfrei NLAN, Giangrisostomi E, Jay RM, et al. Photodriven Transient Picosecond Top-Layer Semiconductor to Metal Phase-Transition in p-Doped Molybdenum Disulfide. Advanced Materials. 2021; 33(14). doi: 10.1002/adma.202006957
41. Xin X, Song Y, Guo S, et al. One-step synthesis of P-doped MoS_2 for efficient photocatalytic hydrogen production. Journal of Alloys and Compounds. 2020; 829: 154635. doi: 10.1016/j.jallcom.2020.154635
42. Xu ML, Tang X, Wang Y, et al. Phosphorus-doped molybdenum disulfide facilitating the photocatalytic hydrogen production activity of CdS nanorod. New Journal of Chemistry. 2019; 43(14): 5335-5340. doi: 10.1039/c9nj00411d
43. Wang L, Xie L, Zhao W, et al. Oxygen-facilitated dynamic active-site generation on strained MoS_2 during photo-catalytic hydrogen evolution. Chemical Engineering Journal. 2021; 405: 127028. doi: 10.1016/j.cej.2020.127028
44. Jaramillo TF, Jørgensen KP, Bonde J, et al. Identification of Active Edge Sites for Electrochemical H_2 Evolution from MoS_2 Nanocatalysts. Science. 2007; 317(5834): 100-102. doi: 10.1126/science.1141483
45. Hinnemann B, Moses PG, Bonde J, et al. Biomimetic Hydrogen Evolution: MoS_2 Nanoparticles as Catalyst for Hydrogen Evolution. Journal of the American Chemical Society. 2005; 127(15): 5308-5309. doi: 10.1021/ja0504690
46. Li Y, Wu S, Zheng J, et al. 2D photocatalysts with tuneable supports for enhanced photocatalytic water splitting. Materials Today. 2020; 41: 34-43. doi: 10.1016/j.mattod.2020.05.018
47. Zhou X, Hao H, Zhang YJ, et al. Patterning of transition metal dichalcogenides catalyzed by surface plasmons with atomic precision. Chem. 2021; 7(6): 1626-1638. doi: 10.1016/j.chempr.2021.03.011
48. Liu J, Liu H, Peng W, et al. High-yield exfoliation of MoS_2 (WS_2) monolayers towards efficient photocatalytic hydrogen evolution. Chemical Engineering Journal. 2022; 431: 133286. doi: 10.1016/j.cej.2021.133286
49. Li X, Sun X, Yu H, et al. Pseudo metallic (1T) molybdenum disulfide for efficient photo/electrocatalytic water splitting. Applied Catalysis B: Environmental. 2022; 307: 121156. doi: 10.1016/j.apcatb.2022.121156
50. Hu X, Jin J, Wang Y, et al. Au/MoS_2 tips as auxiliary rate aligners for the photocatalytic generation of syngas with a tunable composition. Applied Catalysis B: Environmental. 2022; 308: 121219. doi: 10.1016/j.apcatb.2022.121219

51. Parzinger E, Miller B, Blaschke B, et al. Photocatalytic Stability of Single- and Few-Layer MoS_2. ACS Nano. 2015; 9(11): 11302-11309. doi: 10.1021/acsnano.5b04979
52. Peng R, Ma X, Hood ZD, et al. Synergizing plasmonic Au nanocages with 2D MoS_2 nanosheets for significant enhancement in photocatalytic hydrogen evolution. Journal of Materials Chemistry A. 2023; 11(31): 16714-16723. doi: 10.1039/d3ta01657a
53. Zhao X, Chen S, Yin H, et al. Perovskite Microcrystals with Intercalated Monolayer MoS_2 Nanosheets as Advanced Photocatalyst for Solar-Powered Hydrogen Generation. Matter. 2020; 3(3): 935-949. doi: 10.1016/j.matt.2020.07.004
54. Guan W, Li Y, Zhong Q, et al. Fabricating $MAPbI_3/MoS_2$ Composites for Improved Photocatalytic Performance. Nano Letters. 2020; 21(1): 597-604. doi: 10.1021/acs.nanolett.0c04073
55. Khalid NR, Israr Z, Tahir MB, et al. Highly efficient Bi_2O_3/MoS_2 p-n heterojunction photocatalyst for H_2 evolution from water splitting. International Journal of Hydrogen Energy. 2020; 45(15): 8479-8489. doi: 10.1016/j.ijhydene.2020.01.031
56. Song T, Wang J, Su L, et al. Promotion effect of rhenium on MoS_2/ReS_2@CdS nanostructures for photocatalytic hydrogen production. Molecular Catalysis. 2021; 516: 111939. doi: 10.1016/j.mcat.2021.111939
57. Zhang J, Xing C, Shi F. MoS_2/Ti_3C_2 heterostructure for efficient visible-light photocatalytic hydrogen generation. International Journal of Hydrogen Energy. 2020; 45(11): 6291-6301. doi: 10.1016/j.ijhydene.2019.12.109
58. Rothfuss ARM, Ayala JR, Handy JV, et al. Linker-Assisted Assembly of Ligand-Bridged CdS/MoS_2 Heterostructures: Tunable Light-Harvesting Properties and Ligand-Dependent Control of Charge-Transfer Dynamics and Photocatalytic Hydrogen Evolution. ACS Applied Materials & Interfaces. 2023; 15(33): 39966-39979. doi: 10.1021/acsami.3c06722
59. Ou-Yang H, Xu H, Zhang X, et al. Selective-Epitaxial Hybrid of Tripartite Semiconducting Sulfides for Enhanced Solar-to-Hydrogen Conversion. Small. 2022; 18(38). doi: 10.1002/smll.202202109
60. Yanalak G, Koç BK, Yılmaz S, et al. The effect of Ni and Co co-catalysts on the catalytic activity of mesoporous graphitic carbon nitride/black phosphorus/molybdenum disulfide heterojunctions in solar-driven hydrogen evolution. Journal of Environmental Chemical Engineering. 2023; 11(5): 111084. doi: 10.1016/j.jece.2023.111084
61. Peng R, Liang L, Hood ZD, et al. In-Plane Heterojunctions Enable Multiphasic Two-Dimensional (2D) MoS_2 Nanosheets As Efficient Photocatalysts for Hydrogen Evolution from Water Reduction. ACS Catalysis. 2016; 6(10): 6723-6729. doi: 10.1021/acscatal.6b02076
62. Das S, Sharma U, Mukherjee B, et al. Polygonal gold nanocrystal induced efficient phase transition in 2D-MoS_2 for enhancing photo-electrocatalytic hydrogen generation. Nanotechnology. 2023; 34(14): 145202. doi: 10.1088/1361-6528/acade6
63. Xin X, Song Y, Guo S, et al. In-situ growth of high-content 1T phase MoS_2 confined in the CuS nanoframe for efficient photocatalytic hydrogen evolution. Applied Catalysis B: Environmental. 2020; 269: 118773. doi: 10.1016/j.apcatb.2020.118773
64. Liang Z, Xue Y, Wang X, et al. Structure engineering of 1T/2H multiphase MoS_2 via oxygen incorporation over 2D layered porous g-C3N4 for remarkably enhanced photocatalytic hydrogen evolution. Materials Today Nano. 2022; 18: 100204. doi: 10.1016/j.mtnano.2022.100204
65. Zhao Y, Gao J, Bian X, et al. From the perspective of experimental practice: High-throughput computational screening in photocatalysis. Green Energy & Environment. 2024; 9(1): 1-6. doi: 10.1016/j.gee.2023.05.008
66. Xu C, Zhou G, Alexeev EM, et al. Ultrafast Electronic Relaxation Dynamics of Atomically Thin MoS_2 Is Accelerated by Wrinkling. ACS Nano. 2023; 17(17): 16682-16694. doi: 10.1021/acsnano.3c02917
67. Zhou P, Navid IA, Ma Y, et al. Solar-to-hydrogen efficiency of more than 9% in photocatalytic water splitting. Nature. 2023; 613(7942): 66-70. doi: 10.1038/s41586-022-05399-1
68. Zhao Y, Ding C, Zhu J, et al. A Hydrogen Farm Strategy for Scalable Solar Hydrogen Production with Particulate Photocatalysts. Angewandte Chemie International Edition. 2020; 59(24): 9653-9658. doi: 10.1002/anie.202001438
69. Zhai W, Ma Y, Chen D, et al. Recent progress on the long-term stability of hydrogen evolution reaction electrocatalysts. InfoMat. 2022; 4(9). doi: 10.1002/inf2.12357
70. Diyali S, Diyali N, Biswas B. Coordination-driven electrocatalysts as an evolving wave of enthusiasm for sustainable hydrogen production. Coordination Chemistry Reviews. 2024; 500: 215496. doi: 10.1016/j.ccr.2023.215496
71. Zhang J, Wu J, Guo H, et al. Unveiling Active Sites for the Hydrogen Evolution Reaction on Monolayer MoS_2. Advanced Materials. 2017; 29(42). doi: 10.1002/adma.201701955
72. Chen J, Liu G, Zhu Y, et al. Ag@MoS_2 Core–Shell Heterostructure as SERS Platform to Reveal the Hydrogen Evolution Active Sites of Single-Layer MoS_2. Journal of the American Chemical Society. 2020; 142(15): 7161-7167. doi: 10.1021/jacs.0c01649

73. Ekspong J, Sharifi T, Shchukarev A, et al. Stabilizing Active Edge Sites in Semicrystalline Molybdenum Sulfide by Anchorage on Nitrogen-Doped Carbon Nanotubes for Hydrogen Evolution Reaction. Advanced Functional Materials. 2016; 26(37): 6766-6776. doi: 10.1002/adfm.201601994
74. Li H, Tsai C, Koh AL, et al. Correction: Corrigendum: Activating and optimizing MoS_2 basal planes for hydrogen evolution through the formation of strained sulphur vacancies. Nature Materials. 2016; 15(3): 364-364. doi: 10.1038/nmat4564
75. Kim Y, Jackson DHK, Lee D, et al. In Situ Electrochemical Activation of Atomic Layer Deposition Coated MoS_2 Basal Planes for Efficient Hydrogen Evolution Reaction. Advanced Functional Materials. 2017; 27(34). doi: 10.1002/adfm.201701825
76. Kibsgaard J, Chen Z, Reinecke BN, et al. Engineering the surface structure of MoS_2 to preferentially expose active edge sites for electrocatalysis. Nature Materials. 2012; 11(11): 963-969. doi: 10.1038/nmat3439
77. Tsai C, Li H, Park S, et al. Electrochemical generation of sulfur vacancies in the basal plane of MoS_2 for hydrogen evolution. Nature Communications. 2017; 8(1). doi: 10.1038/ncomms15113
78. Liu X, Jiang X, Shao G, et al. Activating the Electrocatalysis of MoS2 Basal Plane for Hydrogen Evolution via Atomic Defect Configurations. Small. 2022; 18(22). doi: 10.1002/smll.202200601
79. Man P, Jiang S, Leung KH, et al. Salt-Induced High-Density Vacancy-Rich 2D MoS_2 for Efficient Hydrogen Evolution. Advanced Materials. 2023; 36(17). doi: 10.1002/adma.202304808
80. Xiao W, Liu P, Zhang J, et al. Dual-Functional N Dopants in Edges and Basal Plane of MoS_2 Nanosheets Toward Efficient and Durable Hydrogen Evolution. Advanced Energy Materials. 2016; 7(7). doi: 10.1002/aenm.201602086
81. Liu P, Zhu J, Zhang J, et al. P Dopants Triggered New Basal Plane Active Sites and Enlarged Interlayer Spacing in MoS_2 Nanosheets toward Electrocatalytic Hydrogen Evolution. ACS Energy Letters. 2017; 2(4): 745-752. doi: 10.1021/acsenergylett.7b00111
82. Yang YQ, Zhao CX, Bai SY, et al. Activating MoS2 basal planes for hydrogen evolution through the As doping and strain. Physics Letters A. 2019; 383(24): 2997-3000. doi: 10.1016/j.physleta.2019.06.036
83. Anjum MAR, Jeong HY, Lee MH, et al. Efficient Hydrogen Evolution Reaction Catalysis in Alkaline Media by All-in-One MoS_2 with Multifunctional Active Sites. Advanced Materials. 2018; 30(20). doi: 10.1002/adma.201707105
84. Lukowski MA, Daniel AS, Meng F, et al. Enhanced Hydrogen Evolution Catalysis from Chemically Exfoliated Metallic MoS_2 Nanosheets. Journal of the American Chemical Society. 2013; 135(28): 10274-10277. doi: 10.1021/ja404523s
85. Yin Y, Han J, Zhang Y, et al. Contributions of Phase, Sulfur Vacancies, and Edges to the Hydrogen Evolution Reaction Catalytic Activity of Porous Molybdenum Disulfide Nanosheets. Journal of the American Chemical Society. 2016; 138(25): 7965-7972. doi: 10.1021/jacs.6b03714
86. Chang K, Hai X, Pang H, et al. Targeted Synthesis of 2H- and 1T-Phase MoS_2 Monolayers for Catalytic Hydrogen Evolution. Advanced Materials. 2016; 28(45): 10033-10041. doi: 10.1002/adma.201603765
87. Zhu J, Wang Z, Yu H, et al. Argon Plasma Induced Phase Transition in Monolayer MoS_2. Journal of the American Chemical Society. 2017; 139(30): 10216-10219. doi: 10.1021/jacs.7b05765
88. Liu Z, Zhao L, Liu Y, et al. Vertical nanosheet array of 1T phase MoS_2 for efficient and stable hydrogen evolution. Applied Catalysis B: Environmental. 2019; 246: 296-302. doi: 10.1016/j.apcatb.2019.01.062
89. Li J, Listwan A, Liang J, et al. High proportion of 1 T phase MoS_2 prepared by a simple solvothermal method for high-efficiency electrocatalytic hydrogen evolution. Chemical Engineering Journal. 2021; 422: 130100. doi: 10.1016/j.cej.2021.130100
90. Yang J, Xu Q, Zheng Y, et al. Phase Engineering of Metastable Transition Metal Dichalcogenides via Ionic Liquid Assisted Synthesis. ACS Nano. 2022; 16(9): 15215-15225. doi: 10.1021/acsnano.2c06549
91. Ekspong J, Sandström R, Rajukumar LP, et al. Stable Sulfur-Intercalated 1T′ MoS_2 on Graphitic Nanoribbons as Hydrogen Evolution Electrocatalyst. Advanced Functional Materials. 2018; 28(46). doi: 10.1002/adfm.201802744
92. Gao B, Zhao Y, Du X, et al. Electron injection induced phase transition of 2H to 1T MoS_2 by cobalt and nickel substitutional doping. Chemical Engineering Journal. 2021; 411: 128567. doi: 10.1016/j.cej.2021.128567
93. Jiang L, Zhang YJ, Luo XH, et al. Se and O co-insertion induce the transition of MoS_2 from 2H to 1T phase for designing high-active electrocatalyst of hydrogen evolution reaction. Chemical Engineering Journal. 2021; 425: 130611. doi: 10.1016/j.cej.2021.130611
94. Guo X, Song E, Zhao W, et al. Charge self-regulation in 1T’’’-MoS_2 structure with rich S vacancies for enhanced hydrogen evolution activity. Nature Communications. 2022; 13(1). doi: 10.1038/s41467-022-33636-8

95. Yang Y, Zhang K, Lin H, et al. MoS_2–Ni_3S_2 Heteronanorods as Efficient and Stable Bifunctional Electrocatalysts for Overall Water Splitting. ACS Catalysis. 2017; 7(4): 2357-2366. doi: 10.1021/acscatal.6b03192
96. Kim M, Anjum MAR, Lee M, et al. Activating MoS_2 Basal Plane with Ni_2P Nanoparticles for Pt-Like Hydrogen Evolution Reaction in Acidic Media. Advanced Functional Materials. 2019; 29(10). doi: 10.1002/adfm.201809151
97. Kim M, Anjum MAR, Choi M, et al. Covalent 0D–2D Heterostructuring of Co_9S_8–MoS_2 for Enhanced Hydrogen Evolution in All pH Electrolytes. Advanced Functional Materials. 2020; 30(40). doi: 10.1002/adfm.202002536
98. Wang S, Zhang D, Li B, et al. Ultrastable In-Plane 1T–2H MoS_2 Heterostructures for Enhanced Hydrogen Evolution Reaction. Advanced Energy Materials. 2018; 8(25). doi: 10.1002/aenm.201801345
99. Cheng Z, Xiao Y, Wu W, et al. All-pH-Tolerant In-Plane Heterostructures for Efficient Hydrogen Evolution Reaction. ACS Nano. 2021; 15(7): 11417-11427. doi: 10.1021/acsnano.1c01024
100. Sun Z, Lin L, Yuan M, et al. Mott–Schottky heterostructure induce the interfacial electron redistribution of MoS_2 for boosting pH-universal hydrogen evolution with Pt-like activity. Nano Energy. 2022; 101: 107563. doi: 10.1016/j.nanoen.2022.107563
101. Li L, Qin Z, Ries L, et al. Role of Sulfur Vacancies and Undercoordinated Mo Regions in MoS_2 Nanosheets toward the Evolution of Hydrogen. ACS Nano. 2019; 13(6): 6824-6834. doi: 10.1021/acsnano.9b01583
102. Zhang W, Liao X, Pan X, et al. Superior Hydrogen Evolution Reaction Performance in 2H-MoS_2 to that of 1T Phase. Small. 2019; 15(31). doi: 10.1002/smll.201900964
103. Hou X, Zhou H, Zhao M, et al. MoS_2 Nanoplates Embedded in Co–N-Doped Carbon Nanocages as Efficient Catalyst for HER and OER. ACS Sustainable Chemistry & Engineering. 2020; 8(14): 5724-5733. doi: 10.1021/acssuschemeng.0c00810
104. Wang X, Zhang Y, Si H, et al. Single-Atom Vacancy Defect to Trigger High-Efficiency Hydrogen Evolution of MoS2. Journal of the American Chemical Society. 2020; 142(9): 4298-4308. doi: 10.1021/jacs.9b12113
105. Ye G, Gong Y, Lin J, et al. Defects Engineered Monolayer MoS_2 for Improved Hydrogen Evolution Reaction. Nano Letters. 2016; 16(2): 1097-1103. doi: 10.1021/acs.nanolett.5b04331
106. Zhan W, Zhai X, Li Y, et al. Regulating Local Atomic Environment around Vacancies for Efficient Hydrogen Evolution. ACS Nano. 2024; 18(14): 10312-10323. doi: 10.1021/acsnano.4c02283
107. Li Y, Zhang R, Zhou W, et al. Hierarchical MoS_2 Hollow Architectures with Abundant Mo Vacancies for Efficient Sodium Storage. ACS Nano. 2019; 13(5): 5533-5540. doi: 10.1021/acsnano.9b00383
108. Ge J, Chen Y, Zhao Y, et al. Activated MoS_2 by Constructing Single Atomic Cation Vacancies for Accelerated Hydrogen Evolution Reaction. ACS Applied Materials & Interfaces. 2022; 14(23): 26846-26857. doi: 10.1021/acsami.2c06708
109. Shi Y, Zhou Y, Yang DR, et al. Energy Level Engineering of MoS_2 by Transition-Metal Doping for Accelerating Hydrogen Evolution Reaction. Journal of the American Chemical Society. 2017; 139(43): 15479-15485. doi: 10.1021/jacs.7b08881
110. Xu J, Shao G, Tang X, et al. Frenkel-defected monolayer MoS_2 catalysts for efficient hydrogen evolution. Nature Communications. 2022; 13(1). doi: 10.1038/s41467-022-29929-7
111. Xiong Q, Wang Y, Liu P, et al. Cobalt Covalent Doping in MoS_2 to Induce Bifunctionality of Overall Water Splitting. Advanced Materials. 2018; 30(29). doi: 10.1002/adma.201801450
112. Xue Y, Bai X, Xu Y, et al. Vertically oriented Ni-doped MoS_2 nanosheets supported on hollow carbon microtubes for enhanced hydrogen evolution reaction and water splitting. Composites Part B: Engineering. 2021; 224: 109229. doi: 10.1016/j.compositesb.2021.109229
113. Li C, Zhu L, Wu Z, et al. Phase Engineering of W-Doped MoS_2 by Magneto-Hydrothermal Synthesis for Hydrogen Evolution Reaction. Small. 2023; 19(48). doi: 10.1002/smll.202303646
114. Kong L, Gao C, Liu Z, et al. Cerium-doped 1 T phase enriched MoS_2 flower-like nanoflakes for boosting hydrogen evolution reaction. Chemical Engineering Journal. 2024; 479: 147725. doi: 10.1016/j.cej.2023.147725
115. Li R, Yang L, Xiong T, et al. Nitrogen doped MoS_2 nanosheets synthesized via a low-temperature process as electrocatalysts with enhanced activity for hydrogen evolution reaction. Journal of Power Sources. 2017; 356: 133-139. doi: 10.1016/j.jpowsour.2017.04.060
116. Zhang P, Xu B, Chen G, et al. Large-scale synthesis of nitrogen doped MoS2 quantum dots for efficient hydrogen evolution reaction. Electrochimica Acta. 2018; 270: 256-263. doi: 10.1016/j.electacta.2018.03.097
117. Ge J, Zhang D, Jin J, et al. Oxygen atoms substituting sulfur atoms of MoS_2 to activate the basal plane and induce the phase transition for boosting hydrogen evolution. Materials Today Energy. 2021; 22: 100854. doi: 10.1016/j.mtener.2021.100854
118. Zhang R, Zhang M, Yang H, et al. Creating Fluorine-Doped MoS_2 Edge Electrodes with Enhanced Hydrogen Evolution Activity. Small Methods. 2021; 5(11). doi: 10.1002/smtd.202100612

119. Shi Y, Zhang D, Miao H, et al. Amorphous/2H-MoS_2 nanoflowers with P doping and S vacancies to achieve efficient pH-universal hydrogen evolution at high current density. Science China Chemistry. 2022; 65(9): 1829-1837. doi: 10.1007/s11426-022-1287-4
120. Li F, Li J, Cao Z, et al. MoS_2 quantum dot decorated RGO: a designed electrocatalyst with high active site density for the hydrogen evolution reaction. Journal of Materials Chemistry A. 2015; 3(43): 21772-21778. doi: 10.1039/c5ta05219j
121. Biroju RK, Das D, Sharma R, et al. Hydrogen Evolution Reaction Activity of Graphene–MoS_2 van der Waals Heterostructures. ACS Energy Letters. 2017; 2(6): 1355-1361. doi: 10.1021/acsenergylett.7b00349
122. Zhang CL, Xie Y, Liu JT, et al. 1D Core−Shell MOFs derived CoP Nanoparticles-Embedded N-doped porous carbon nanotubes anchored with MoS_2 nanosheets as efficient bifunctional electrocatalysts. Chemical Engineering Journal. 2021; 419: 129977. doi: 10.1016/j.cej.2021.129977
123. Zhang X, Yang P, Jiang SP. Ni diffusion in vertical growth of MoS_2 nanosheets on carbon nanotubes towards highly efficient hydrogen evolution. Carbon. 2021; 175: 176-186. doi: 10.1016/j.carbon.2021.01.010
124. Yu H, Xue Y, Hui L, et al. Controlled Growth of MoS_2 Nanosheets on 2D N-Doped Graphdiyne Nanolayers for Highly Associated Effects on Water Reduction. Advanced Functional Materials. 2018; 28(19). doi: 10.1002/adfm.201707564
125. Hui L, Xue Y, He F, et al. Efficient hydrogen generation on graphdiyne-based heterostructure. Nano Energy. 2019; 55: 135-142. doi: 10.1016/j.nanoen.2018.10.062
126. Song L, Zhang X, Zhu S, et al. Hydrogen spillover effect enhanced by carbon quantum dots activated MoS_2. Carbon. 2022; 199: 63-69. doi: 10.1016/j.carbon.2022.07.071
127. Attanayake NH, Abeyweera SC, Thenuwara AC, et al. Vertically aligned MoS_2 on Ti_3C_2 (MXene) as an improved HER catalyst. Journal of Materials Chemistry A. 2018; 6(35): 16882-16889. doi: 10.1039/c8ta05033c
128. Wu X, Wang Z, Yu M, et al. Stabilizing the MXenes by Carbon Nanoplating for Developing Hierarchical Nanohybrids with Efficient Lithium Storage and Hydrogen Evolution Capability. Advanced Materials. 2017; 29(24). doi: 10.1002/adma.201607017